International Journal of Hydrogen Energy 137 (2025) 961–975

Contents lists available at ScienceDirect

International Journal of Hydrogen Energy

journal homepage: www.elsevier.com/locate/he

Novel Ni–Ru/CeO_2 catalysts for low-temperature steam reforming of methane

G. Sorbino [a], A. Di Benedetto [b], C. Italiano [c], M. Thomas [c], A. Vita [c], G. Ruoppolo [a], G. Landi [a,*]

[a] Institute of Science and Technology for Sustainable Energy and Mobility - CNR, Naples, Italy
[b] Dipartimento di Ingegneria Chimica, Dei Materiali e Della Produzione Industriale – Università Degli Studi di Napoli Federico II, Naples, Italy
[c] Institute for Advanced Energy Technologies of the National Research Council (CNR-ITAE), Via S. Lucia Sopra Contesse 5, 98126, Messina (ME), Italy

ARTICLE INFO

Handling Editor: Ibrahim Dincer

Keywords:
Methane steam reforming
Hydrogen
Low temperature
Nickel
Ceria
Ruthenium

ABSTRACT

Upgrading of biogas and biomethane into H_2-rich streams by steam reforming is regarded as an effective strategy to reduce fossil fuel consumption contributing to the transition towards a green energy system. In this context, novel reactor configurations such as membrane reactors appear a promising route for process intensification, but they require novel catalysts more active at low temperatures, stable, and resistant to coke formation. In this work, we prepared and tested structured catalysts characterized by a low Ni content (7 wt%) and a very low Ru content (≤1 wt%) supported on ceria and deposed onto SiC monoliths. Catalysts were tested at low temperatures (<600 °C), i.e. at temperatures suitable for applications in Pd-based membrane reactors. Fresh and used catalysts were characterized by ICP-MS, N_2 physisorption, XRD, TEM, SEM-EDS, XPS and H_2-TPR to identify the physicochemical properties affecting the catalytic activity. The catalysts showed good activity towards methane reforming, stable performance, and good resistance to coke formation. Ruthenium affects both the intrinsic catalytic activity and the resistance to the inhibiting effect of steam on the reaction rate. This is related to improved redox properties due to the intimacy between the active metals and their strong-metal-support-interaction with the ceria. Finally, our catalysts show self-activation under reaction conditions, which is an interesting property for applications.

1. Introduction

Hydrogen is a crucial energy carrier, and its production from both fossil and renewable sources is pivotal for the future energy system [1]. Currently, hydrogen production is predominantly performed using fossil sources, primarily methane gas in the steam methane reforming (SMR) process. An intriguing topic is the enhancement of the value of biogas and biomethane, as effective means to reduce fossil fuel consumption and contribute to the transition towards a green energy system [2], that can be converted into H_2-rich streams by steam reforming as well.

In the energy transition phase, blue hydrogen (by steam reforming of natural gas) is the short-to-medium-term opportunity, while green hydrogen represents the long term solution [3]. Moreover, by replacing natural gas with biogas or biomethane, hydrogen production characterized by low (or even negative through CCS) carbon emissions can be achieved.

Reforming reactions, as endothermic reactions, are thermodynamically favored at high temperatures and occur with an increase in the number of moles, making them favorable at low pressures. Moreover, the carbon monoxide content in the exiting stream is relatively high and, consequently, it has to be reduced through the two water gas shift (WGS) stages and a purification stage. To simplify the process scheme novel reactor configurations have been explored. In particular, simultaneous hydrogen separation in membrane reactors has been proposed [4]. In these reactors, thanks to the removal of hydrogen through membranes, the thermodynamic equilibrium of the reaction is shifted towards the products and then the same or even higher conversions can be achieved with respect to the traditional process [5–7].

Studies on membrane reactors for methane reforming have focused on palladium-based membranes due to their high-temperature application and hydrogen selectivity at 99.99% [4,5]. However, the limitations of palladium-based membranes in reforming processes are mainly related to their long-term instability, especially at temperatures exceeding 600 °C.

In this context, the development of novel catalysts more active at low temperatures can pave the way for the development of effective

* Corresponding author.
E-mail address: gianluca.landi@stems.cnr.it (G. Landi).

https://doi.org/10.1016/j.ijhydene.2024.07.385
Received 27 February 2024; Received in revised form 1 July 2024; Accepted 25 July 2024
Available online 1 August 2024

processes based on membrane reactors.

Nickel-based catalysts have been the most used catalysts due to their high catalytic activity, good availability and relatively low price [8,9]. Despite their long application in traditional methane steam reforming processes, some of the major issues including sintering, carbon deposition, and sulphur poisoning still need to be investigated [10–13]. Many innovative strategies have been developed recently to overcome some of these challenges, such us the addition of promoters, including noble metals (Pt, Ru, Rh) [14–19], and coinage metals (Au, Ag, and Cu) [11, 20–23], and alkali metals (K) [24], the former being the most active systems.

In this respect, bi/polymetallic catalysts gained increasing attention in recent years [9,11,25], and the synergistic effect has been studied experimentally and numerically, also by combining doping and supporting on "non-traditional" supports. For instance, Ru–Ni catalysts have been tested by Jeong et al. [26] to study the promoting effect of Ru to Ni/Al_2O_3 and Ni/$MgAl_2O_4$ systems A small amount of Ru significantly improved the fouling resistance and redox properties of nickel, especially on Ni/$MgAl_2O_4$. Similarly, Li and co-workers carried out several studies on the doping effect of noble metals (Ru, Rh, Pt, and Pd) on Ni/Mg(Al)O catalysts in a daily start-up and shut-down operation [27–32]. Noble metal doping improved the reducibility of the catalyst by affecting nickel reduction temperature and oxygen release. However, there is not a consensus on the positive effect of Ru. In fact, Morales-Cano et al. [16] showed that, while Rh and Ir form Rh–Ni and Ir–Ni alloy that could enhance both the activity and sintering resistance of Ni/Al_2O_3, the formation of Ru–Ni is more difficult due to the lower miscibility of Ru in Ni. Kim et al. [33] demonstrated that Ru addition increased the stability of Ni catalyst by enhancing Ni dispersion and reducibility due to the interaction between metals and hydrogen spillover from Ru. Similar results were reported by Fazlikeshteli et al. [34], according to which, the greater synergy between Ni and Ru led to higher activity and stability of the RuNi/CeO_2 catalyst towards the catalytic partial oxidation of methane.

The catalyst activity and resistance to coke formation are also significantly affected by the support material [35–37]. The most commonly supports (Al_2O_3, CeO_2, ZrO_2, TiO_2, MgO) are usually required to overcome the rapid Ni-based catalyst deactivation, improve the activity and stability of the catalysts, enhance catalyst resistance to oxidation, improve thermal stability and mechanical strength [38]. As reviewed by Manan et al. [39], many studies revealed that catalysts containing or supported on ceria exhibit superior performance due to the ceria excellent redox properties and oxygen storage capacity. As a matter of fact, CeO_2 can readily release lattice oxygen species through reduction from Ce^{4+} to Ce^{3+}, promoting the oxidation of intermediate carbon species [39]. The reasons for the great interest in ceria include not only its excellent redox capacity, and remarkable oxygen storage and release capabilities but also its environmental compatibility. García--Vargas et al. [40] showed that Ni/CeO_2 had better catalytic activity, stability, and conversion rates than Ni/Al_2O_3 due to its higher reducibility. Moreover, the oxygen vacancies and Ce^{3+} cations formed under reducing atmosphere activate C–O bonds dissociation and promote CO_2 activation on the nickel sites close to the interface between the metal and the support [41–43]. This reduces the deposition of carbon deposits and promotes catalyst stability during the methane reforming process.

Combining doping with ruthenium and supporting on ceria appears an interesting strategy to further improve the catalytic properties of Ni-based catalysts towards methane steam reforming in terms of intrinsic activity, stability, and resistance to coking. It is worth noting that ruthenium is the cheapest among the noble metals [44]. Moreover, issues related to sintering and unmixing of Ni and Ru, should not be detected at low temperatures, typical of membrane reactors. Zakrzewski et al. [454] demonstrated that the simultaneous presence of Ru and CeO_2 promotes the activity of Ni/Al_2O_3 catalyst due to the formation of Ru–Ni clusters, the greater Ni dispersion, and the presence of Ru particles themselves acting as active sites. However, the Authors did not investigate the effect of Ru loading (fixed at 1 wt%); moreover, Ni content was high (20 wt%) and the stability of this catalyst was not tested.

The aim of the present work is to evaluate the effect of Ru loading on Ni catalysts supported on ceria with low Ni content (7 wt%) towards methane steam reforming. More specifically, the low-temperature activity ($T < 600$ °C) will be investigated for applications in membrane reactors. Catalytic activity was studied on structured catalysts. The active phase was dispersed onto SiC monoliths, exhibiting high thermal conductivity and mechanical resistance, low specific weight, and chemical inertia. It is worth noting that recovery of the active phase is extremely easy through acid or basic washing, reducing the investment cost of the process for the final disposal of the spent catalyst and the full reuse of the support [46]. In addition, the use of monolith-based catalysts for reforming reactions could improve catalytic performance providing many advantages such as high surface-to-volume ratio, low pressure drop, good mass and heat transfer [47,48]. Fresh and used catalysts were characterized by several techniques (ICP-MS, N_2 physisorption, XRD, TEM, SEM-EDS, XPS, H_2-TPR) to identify the physicochemical properties affecting the catalytic activity. Specific transient reaction tests were carried out to highlight the role of ruthenium in the reaction mechanism.

2. Materials and methods

2.1. Catalyst preparation

Both structured and reference powder catalysts were prepared according to the procedures reported in Section S.1.1 (Supplementary materials). Table 1 shows the compositions of the prepared catalysts and the corresponding labels.

Before catalytic tests, catalyst reduction with H_2 is expected to convert nickel oxide into its metallic form, which is the actual active phase [49]. In this work, the catalysts will be tested without a pre-reduction step.

2.2. Activity tests

The structured catalysts (composed of 3 g of SiC and approximately 1.1 g of Ni–Ru/CeO_2) were tested in the experimental setup described elsewhere [50]. A detailed description is reported in Section S.1.2 (Supplementary Materials).

Catalytic tests were performed at fixed contact time, defined as the (catalyst weight)/(flow rate) ratio and equal to 0.08 g s cm^{-3}. The reaction temperature varied from 450 to 550 °C.

The effects of temperature and feed composition on methane conversion were calculated as:

$$x_{CH_4} = \frac{CH_4^{IN} - CH_4^{OUT}}{CH_4^{IN}}$$

where CH_4^{IN} and CH_4^{OUT} are the inlet and outlet methane concentrations measured by the analysis system on dry basis. Due to the high dilution of gaseous streams used in this work, the change of the total mole number

Table 1
Labels, nominal compositions (wt. %), specific surface areas (SSA; $m^2\ g^{-1}$) of the prepared catalysts.

Sample	Ni	Ru	SSA
Ni	7.0	–	29
NiRu0.2	7.0	0.2	32
NiRu0.5	7.0	0.5	32
NiRu0.7	7.0	0.7	27
NiRu1.0	7.0	1.0	26
Ru1.0	–	1.0	25

* Weight percentages are reported with respect to the weight of the active phase.

can be considered negligible, i.e. the overall flow rate can be considered constant independently from the methane conversion. The carbon mass balance (MB_C) was calculated as:

$$MB_C = \frac{CH_4^{IN} - \left(CH_4^{OUT} + CO_2^{OUT} + CO^{OUT}\right)}{CH_4^{IN}}$$

where CO_2^{OUT} and CO^{OUT} are the outlet CO_2 and CO concentrations measured by the analysis system on dry basis. Carbon balance was closed within ±5%.

CO conversion was defined and calculated as:

$$x_{CO}^{WGS} = \frac{CO^{IN,SR} - CO^{OUT}}{CO^{IN,SR}}$$

where $CO^{IN,SR}$ is the concentration of CO produced solely from the steam reforming of methane, following the stoichiometry of eq. (1), i.e.:

$$CO^{IN,SR} = x_{CH_4}\ CH_4^{IN}$$

Cyclic reduction and oxidation tests were conducted on the reference powder catalysts in the experimental setup described in Ref. [51]. A detailed description is reported in Section 1.2 (Supplementary Materials). Each cycle involves an oxidation phase, in which the sample is exposed to a stream of water vapor in nitrogen, and a reduction phase, in which a methane/nitrogen stream is fed onto the oxidized sample. The composition of the feed mixture is 8% H_2O in N_2 and 4% CH_4 in N_2 at constant temperature (500 °C) and contact time is equal to 0.09 g s cm^{-3}. Each test is composed of two cycles. The amount of consumed and produced species were calculated by the numerical integration of the concentration profiles measured at the reactor outlet (integration performed by OriginPro 8.5 software) and then calculating the moles of each species according to the following equations:

$$A_i = \int_{t_i}^{t_f} c_i(t)dt$$

$$n_i = \frac{F \bullet A_i \bullet P}{100 \bullet R \bullet T}$$

Where A_i is the area (vol%·s) of the concentration profile of the i species, t_i and t_f (s) are the initial and final integration time respectively, $c_i(t)$ (vol%) is the concentration of the i species at time t (for reactants $c_i(t)$ is equal to c^0-$c_j(t)$, where c^0 is the feed concentration and $c_j(t)$ is the measured concentration at time t), n_i (mol) is the amount of consumed/produced species, F (l/s) is the total flow rate (measured at atmospheric pressure and temperature), P (atm) is the atmospheric pressure, R (atm·l·mol^{-1}·K^{-1}) is the universal gas constant, T (K) is the atmospheric temperature.

Equilibrium calculations were performed using Aspen Plus (AspenTech). The equilibrium was calculated using Gibbs free energy under the specified operating conditions.

2.3. Materials characterizations

The fresh and used catalysts were characterized using ICP-MS, SEM-EDS, XRD, N_2-physisorption, NH_3-TPD, CO_2-TPD, H_2-TPR, and TEM analysis. The catalyst composition was determined by ICP-MS analysis using an Agilent 7500CE instrument. The results (Table S2) show that the measured metallic contents correspond to the nominal values within the experimental error.

The internal morphology of monolith channels was observed using an FEI Inspect scanning electron microscope (SEM) equipped with an energy dispersive X-ray (EDX) probe for the elemental mapping.

XRD spectra were collected with an XRD diffractometer, PANalytical X'Pert Pro. The measurements were carried out with a step size of 0.02° and a counting time of 80 s per step.

Brunauer-Emmett-Teller (BET) SSA of fresh and used materials were measured by N_2 adsorption at 77 K with a Quantachrome Autosorb-1C instrument after degassing the samples at 150 °C for 1.5 h.

Temperature-programmed desorptions of ammonia (NH_3-TPD) and carbon dioxide (CO_2-TPD) were performed by a Micromeritics Autochem II 2020 (Micromeritics, Norcross, GA, USA) equipped with a TC detector (Norcross, GA, USA). profiles were deconvolved using Origin 8.5 software.

Temperature-Programmed Reduction (TPR) was performed on the reference powder catalysts in the same test rig used for steady-state and cyclic experimental tests on powder samples. All the catalysts were pretreated in a 20 vol% O_2/N_2 stream at 600 °C. During TPR, catalysts were reduced in a 2 vol% H_2/N_2 mixture (flow rate: 35 Nl/h) heating up to 600 °C (heating rate: 10 °C/min). Temperature-Programmed Oxidation (TPO) was carried out on structured catalysts at the end of the experimental campaign. During TPO, the used catalysts were exposed to a 2 vol% O_2/N_2 stream (flow rate: 35 Nl/h) heating up to 600 °C (heating rate: 10 °C/min). Reduction and oxidation profiles were deconvoluted using OriginPro 8.5 software.

High-resolution transmission electron microscopy (HR-TEM) and energy-dispersive X-ray spectroscopy (EDX) mapping images were obtained using a cold field transmission electron microscope (JEM-F200, Jeol, Japan) at an operating voltage of 200 kV.

X-ray photoelectron spectroscopy (XPS) was conducted on a SPECS system equipped with a XR50 source operating at 150 W and a Phoibos 150 MCD-9 detector. The analysis chamber was maintained at a pressure below 10−7 Pa. The binding energy (BE) values were measured with pass energy of 25 eV and energy step of 0.1 eV. Quantification of surface composition was based on the peak fitting and normalization of Ni (2p 3/2), Ce (3d 5/2 and 3/2), Ru (3p 3/2), and O1s primary peaks.

3. Results

3.1. Characterizations

The BET surface areas of the fresh samples are given in Table 1. In comparison to the support (ceria: 137 m^2g^{-1}) [52], the specific surface areas (SSAs) of the prepared catalysts are markedly lower. This is due the heat treatment at 550 °C; in fact, pure ceria nanoparticles calcined at 550 °C show an SSA equal to 35 m^2/g. Used samples exhibit SSA similar to the fresh ones, suggesting that no structure changes occur under reaction conditions.

SEM/EDS results on Ni and NiRu0.7 are reported in Figure S4 (Supplementary Materials). Images recorded on other samples are similar and are not reported. Continuous distribution of ceria is detected, suggesting the penetration of ceria into the SiC walls. This is due to the nanometric size of ceria, whose characteristic dimension is significantly lower than that of SiC pores (11 μm) [53].

Metals distribution along the channel appears quite homogeneous with a good overlap of Ni and Ru. This means that a segregation of the metals cannot be observed. However, a detailed discussion of their interaction requires a deeper investigation.

The XRD patterns of fresh catalysts (shown in Figure S5) show typical peaks of fluorite structure with reflections at 2θ = 28.7°, 32.9°, 47.5°, and 56.0° (JCPDS card n° 43–1002), as expected for CeO_2 systems. No diffraction peak due to ruthenium oxide was detected.Only peaks attributed to the ceria structure are observed on the Ru1.0 sample. On all other samples, diffraction peaks related to nickel oxide were also detected, with reflections at 2θ = 37.3°, 43.3°, 62.9° (JCPDS card n° 04–0835).

In Table 2, quantitative XRD analysis data for the fresh samples are presented. In the mixed samples, an increase in the Ru content is accompanied by an increment in the cell parameter of ceria. This suggests that a portion of Ru may be incorporated into the fluorite structure, leading to increased distortion. Concerning NiO, there is no observed difference in the cell parameter with the increase in Ru content, whereas a noticeable difference appears in the crystallite size of NiO, suggesting

Table 2
Quantitative XRD analysis of fresh samples.

Sample	CeO_2		NiO		
	2θ (°)	**d (nm)**	**2θ (°)**	**d (nm)**	**τ (Å)**
Ni	28.633	0,31175	43,31	0,20893	5,00
NiRu0.2	28.639	0,31169	43,27	0,20909	6,02
NiRu0.5	28.623	0,31186	43,34	0,20877	4,58
NiRu0.7	28.623	0,31186	43,36	0,20868	3,70
NiRu1.0	28.596	0,31214	43,26	0,20916	6,36
Ru1.0	28.679	0,31126	–	–	–

an increase in dispersion with the rise in Ru content up to 0.7%, in agreement with previous works [53].

In Figure S6, the XRD pattern of the fresh and used NiRu0.2 catalyst is shown as representative of all other catalysts. The fluorite structure remains unchanged in the used catalyst, but the peaks associated with NiO disappear, and those related to metallic Ni (2θ = 44.5°, 51.86°; JCPDS card n° 04–0850) arise. In the used sample, the interplanar distance of ceria is 0.3123 nm. The crystallite size of Ni is comparable to that of the initial NiO, suggesting that there is no redistribution of Ni following the reaction.

Low-magnification (a-c,g-i) and high-magnification (d-f,j-l) HR-TEM images of used samples are shown in Fig. 1. All samples exhibited

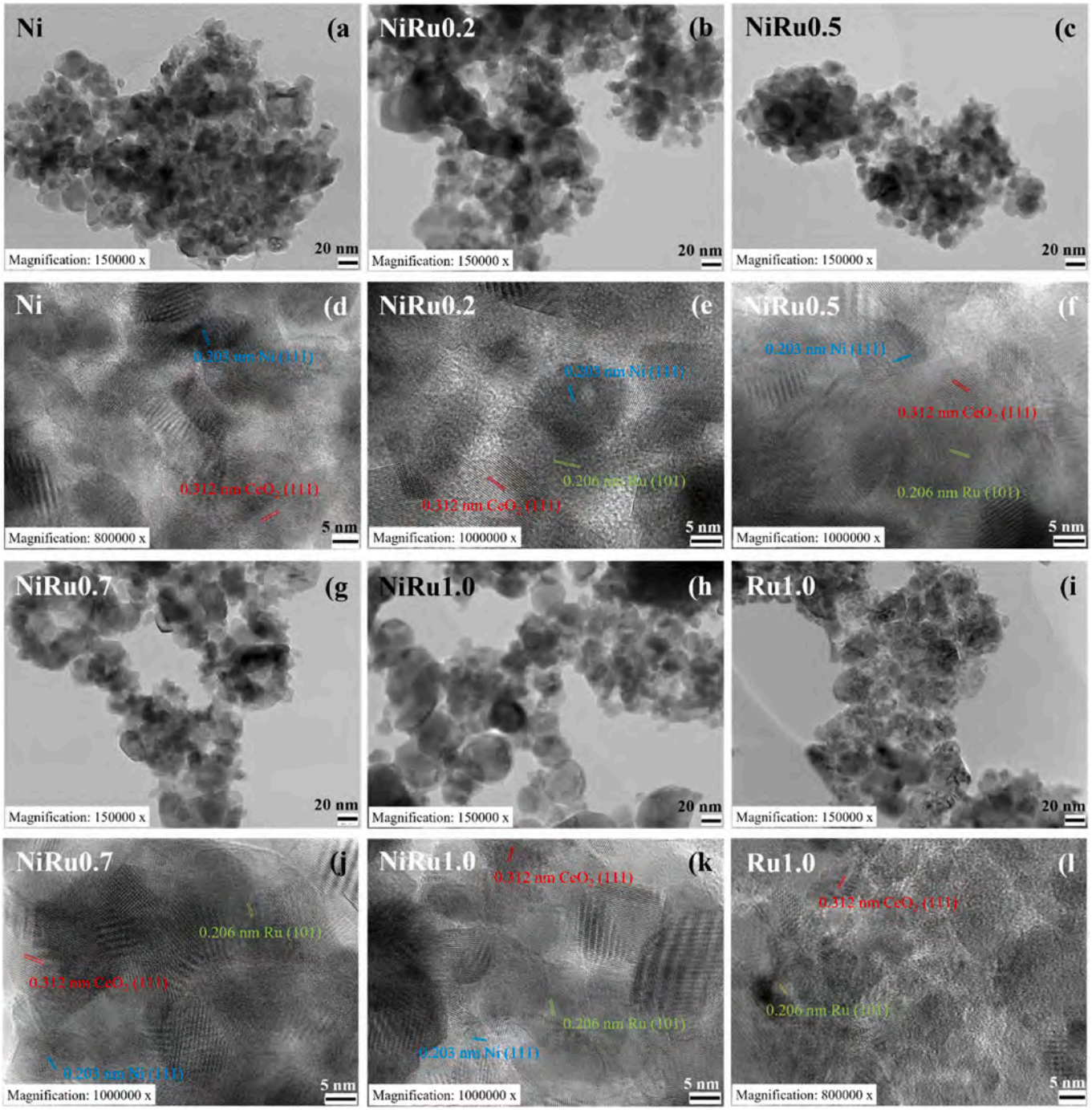

Fig. 1. Low-magnification (a-c,g-i) and high-magnification (d-f j-l) HR-TEM images of (a,d) Ni, (b,e) NiRu0.2, (c,f) NiRu0.5, (g,j) NiRu0.7, (h,k) NiRu1.0, and (i,l) Ru1.0 catalysts.

agglomerates of almost spherical nanoparticles, which form a mesoporous network. High-magnification TEM images in Fig. 1d–f,j-l display a variety of lattice fringes with an average interplanar spacing of 0,312, 0,203 and 0,206 nm, indexed to the mainly exposed (111) crystal planes of CeO_2 (JCPDS card no. 431002), (111) crystal planes of Ni (JCPDS card no. 040850), and (101) crystal planes of Ru (JCPDS card no. 060663), respectively. Overall, these observations are consistent with the XRD analysis (Figure S5). The dispersion and interaction of metallic nanoparticles, as well as the elemental distribution across the catalytic samples, were further investigated through additional TEM analysis. Fig. 2 shows HR-TEM images (a-c), coupled with STEM-EDX elemental mapping (d-h) of used NiRu0.7 catalyst. The latter is essential to provide valuable information about the location of the catalytically active Ni and noble metal (Ru) phases and, consequently, about the presence of Ni–Ru alloy formation [54]. The composition based on the EDX data was found to be 1.7 wt% (Ru), 23.1 wt% (Ni), and 47.9 wt% (Ce), quite in accordance with the nominal composition and signal of a high Ru distribution on the CeO_2 support. As a first evidence, Ru is located both on the CeO_2 support and on the metallic Ni-rich particles (Fig. 2f–h). Moreover, it appears to be present as small Ru clusters (10–20 nm) or even as highly dispersed Ru single atoms (Fig. 2h). Ru clusters appear to be closely attached to the Ni phase (Fig. 2g and h), resulting in the formation of substantial inter-element interfaces [55]. However, the partial existence of Ru as Ni–Ru alloy or heterostructure could not be excluded due to the high overlap between Ru single atoms and Ni phase (Fig. 2f–h). Our observations agree with literature results previously reported for Ni–Ru bimetallic catalysts [54,56,57].

XPS was performed to investigate the chemical composition and the environment at the surface of the as-prepared NiRu0.7 catalyst. The XPS spectra of the Ce3d region (Fig. 3a) is deconvoluted into ten peaks, whose energies are the typical values for Ce(IV) and Ce(III). The peaks denoted as v (881.3 eV), v'' (887.9 eV), v''' (897.2 eV), u (899.7 eV), u'' (906.4 eV), and u''' (915.2 eV) are attributed to the Ce^{4+} species, while v^0 (878.8 eV), v' (883.8 eV), u^0 (898.7 eV), and u' (902.3 eV) correspond to Ce^{3+} species [58–61]. The ratio of Ce^{3+} ion peaks area to that of the total Ce^{3+} and Ce^{4+} ions peaks area, revealed that ca. 11% of the ceria surface consisted of Ce3þ species. This could be ascribed to the formation of oxygen vacancies into the ceria lattice caused by the insertion of metal Ru cations, in accordance with XRD results [61,62]. The XPS spectra in the O1s region (Fig. 3b) showed two distinct peaks ascribable to the surface lattice oxygen (O_α, 528.3 eV) and the surface hydroxyl groups or adsorbed oxygen (O_β, 529.7 eV) [63,65]. The Ni2p spectra (Fig. 3c) is deconvoluted into three peaks: two adjacent bands with maximum at 852.9 eV and 854.6 eV, labelled as Ni(II) and Ni(II)*, and a broad satellite peak at 860.2 eV, consistent with the presence of Ni2+ species [64,66]. This double peaked structure suggess the presence of surface Ni species with different environments. In particular, the peak at highest binding energy (Ni(II)) was ascribed to presence of NiO highly dispersed on the support surface which created higher metal-support interaction. Instead, the second feature on the low binding-energy side (Ni(II)*) belonged to bigger NiO particles, being their photoemission affected by the presence of Ni cations as next-nearest neighbors [67,68]. Moreover, no peak corresponding to reduced nickel (Ni^0) was detected (Fig. 3c), suggesting that Ni species were almost not reduced under the adopted conditions, in agreement with XRD results (Figure S5).The Ru 3p XPS spectra were analyzed due to the difficulty in distinguishing Ru3d signal from C1s signal. The fitting revealed the presence of four peaks, the two located at 462,2 and 484.4 eV corresponded to Ru in the zero valence state whereas the other two at 464.3 and 486.3 eV evidenced the presence of Ru at high valence state, Ru(IV) [63,64,69].

3.2. Temperature programmed measurements

Powder samples were used to evaluate the redox properties. Each sample underwent a Temperature-Programmed Reduction (TPR) in hydrogen. It is essential to emphasize that the activity tests presented in the following sections were performed on calcined catalysts without any reducing pretreatment, which is typical for nickel catalysts used in steam reforming [70].

To evaluate the actual oxidation state of nickel and ruthenium under reaction conditions, TPR after a reaction test was conducted on the powder catalysts. Before the reaction tests, each sample was pretreated in a 20 vol% O_2/N_2 stream to ensure the full oxidation of metals. A reaction test is then carried out on powder samples in the experimental rig used for H_2-TPR measurements under the same reaction conditions reported in Section 3.3, followed by an H_2-TPR to identify any differences between pre- and post-reaction states. It is worth noting that the catalytic performance obtained on the powder samples are comparable with those reported in Section 3.3.

On the fresh Ni sample (Fig. 4 left), a single reduction peak is observed at 330 °C, associated with the reduction of nickel oxide into its respective metallic state [71]. Hydrogen consumption on the used Ni sample (Fig. 4 left) is negligible, suggesting its full reduction under the reaction conditions.

On the Ru1.0 sample (Fig. 4 right), a single reduction peak is observed at 122 °C, associated with the transition from ruthenium oxide (RuO_2) to metallic ruthenium (Ru) [72]. As occurred on Ni, the used sample does not undergo measurable reduction, suggesting that it is fully reduced under the reaction mixture.

The corresponding hydrogen consumptions are given in Table 3. The ratio of actual to theoretical H_2 consumption is greater than 1, suggesting that the reduction degree of the two monometallic catalysts is greater than 100%. The observed "over-reduction" of the sample may be addressed to the reduction of the ceria beyond that of Ni and/or Ru oxides [73,74].

For the "mixed" fresh catalysts, Fig. 5 shows two reduction peaks, at low (~100 °C) and high temperature (~300 °C), both slightly lower than those corresponding to the peaks of the two monometallic catalysts. This result suggests a synergistic behavior, since each metal slightly increases the reducibility of the other, in agreement with literature results [71,73,75]. The high intimacy between Ni and Ru clusters shown by TEM results, explains the enhanced Ni reducibility in the bimetallic system.

As shown in Table 3 and Figure S7, even for the bimetallic catalysts, the H_2/H_{2_t} ratio is greater than 1, due to ceria contribution. Table 3 and Figure S7 show the ratios between the actual H_2 consumption of each peak and the theoretical consumptions due to the complete reduction of Ru (H_2/H_{2_Ru}) and Ni (H_2/H_{2_Ni}). Interestingly, at low Ru content higher H_2/H_{2_Ru} ratios are measured; this can be related to a higher Ru dispersion, thus significantly improving Ru-ceria interaction. On the other hand, H_2/H_{2_Ni} is quite constant with a slight increase at high Ru loads, confirming the beneficial effect of metallic Ru on the Ni reducibility, due to the high intimacy detected by TEM. Thus, the improved redox properties of NiRu catalysts can be addressed to both metal-metal interaction and to metal-ceria interaction, in accordance with XRD and XPS results. The latter is a well-known phenomenon, reported in the literature as strong-metal-support-interaction (SMSI) [76] and electronic metal support interaction (EMSI) [77].

TPR analysis conducted on used powders (Fig. 5) shows a marginal H_2 consumption at low temperatures, while the high-temperature peak disappears, indicating no H_2 consumption due to NiO reduction, in agreement with the XRD results. This result suggests that, under reaction conditions, the catalyst tends to self-reduce to the metallic phases, which are active for the steam reforming reaction, confirming the self-activation of the proposed catalysts. This phenomenon is reported in the literature [26,53,74], but our catalysts show self-reduction under milder conditions.

It is worth noting that the powder catalyst undergoing activity tests showed methane conversions and product distributions comparable to those found in activity tests on the monoliths (see Section 3.3).

Selected used catalysts (Ni, Ru1.0, and NiRu1.0) were further characterized by NH_3 and CO_2 TPD to titrate both acid and basic sites.

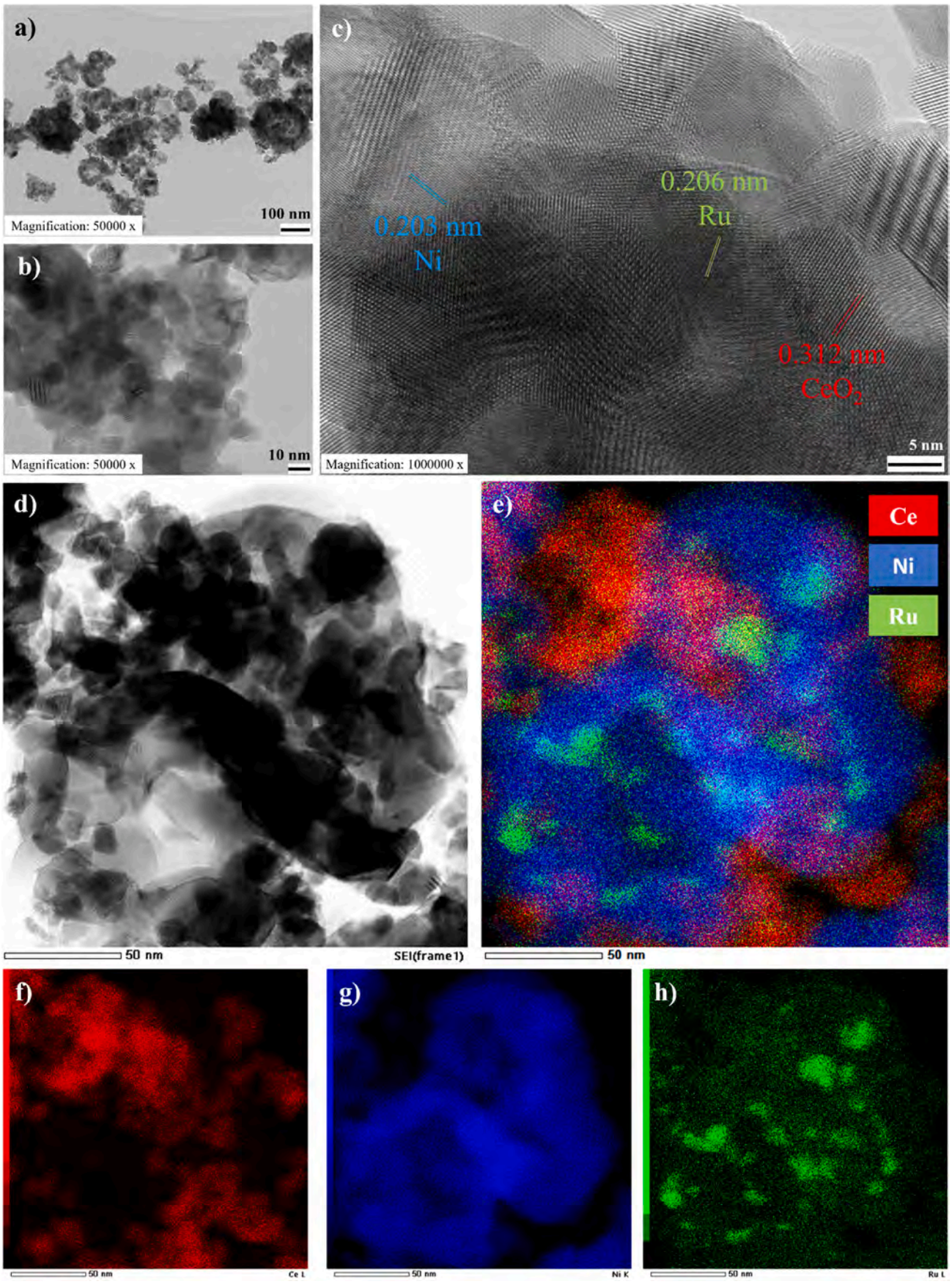

Fig. 2. HR-TEM images at different magnifications (a–c), bright-field image (BFI, d), and EDX elemental mapping (e-h) of NiRu0.7 catalyst.

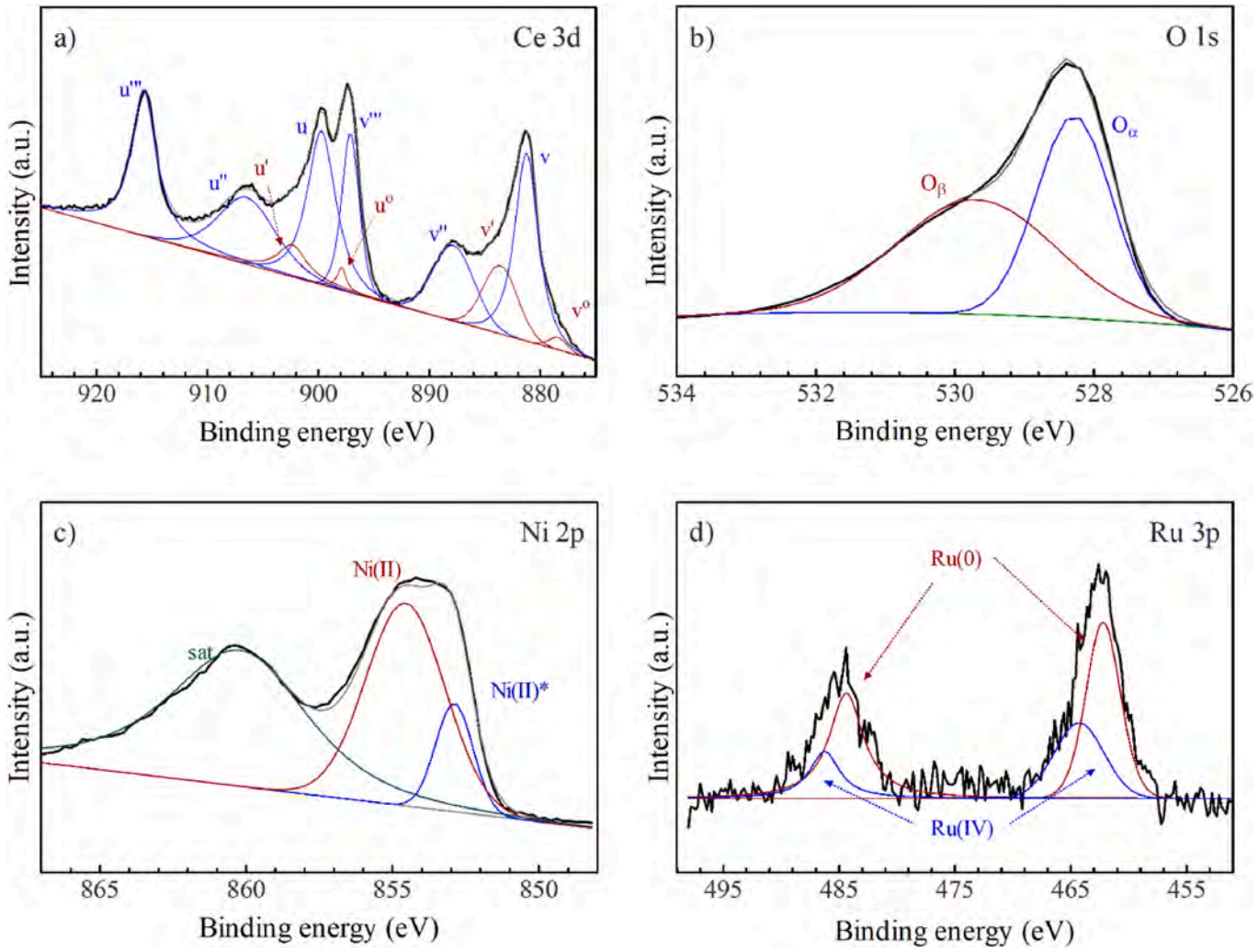

Fig. 3. XPS spectra of Ce 3d, O 1s, Ni 2p, and Ru 3p regions of as-prepared NiRu0.7 sample.

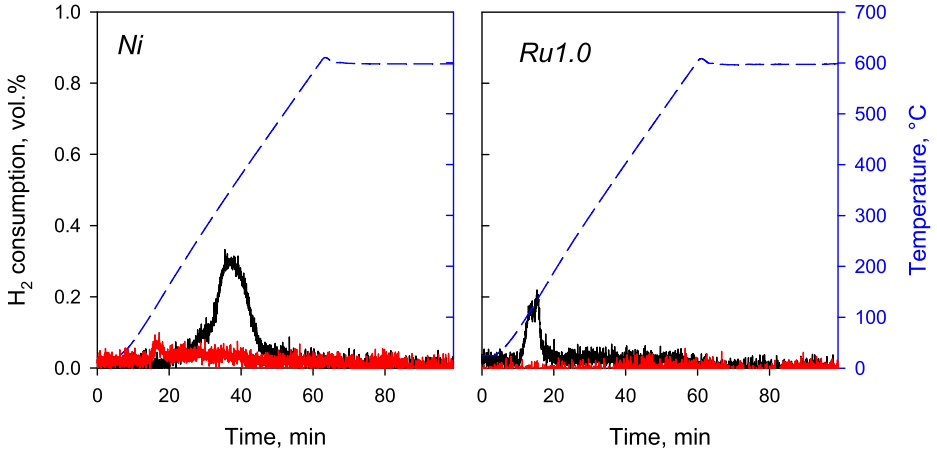

Fig. 4. H_2-TPR profiles on fresh (black lines) and used (red lines) Ni and Ru1.0 catalysts. (For interpretation of the references to colour in this figure legend, the reader is referred to the Web version of this article.)

Desorption profiles are reported in Figure S8, while desorbed amounts are reported in Table 4.

According to Refs. [78,79], weak, medium, and strong acidity are related to desorption peaks at temperatures <300 °C, 300–500 °C, and >500 °C respectively. NH_3 desorption profiles (Figure S8, bottom) show a pronounced low temperature acidity on both Ni-containing catalysts. The medium acidity is very different among the samples. Ni shows a very large desorption peak, which is significantly reduced on NiRu1.0. On Ru1.0 a wider desorption peak, centered at higher temperatures, is detected. NiRu1.0 shows the larger amount of strong acid sites, which

Table 3
Peak temperatures (°C), H_2 uptakes (mmol/g), and ratios between actual and theoretical H_2 consumptions for fresh catalysts.

Sample	T[a]	T [b]	H_2 uptake[a]	H_2 uptake [b]	H_2/H_{2_t}	H_2/H_{2_Ru}	H_2/H_{2_Ni}
Ni	/	330	/	1.70	1.43	/	1.43
NiRu0.2	113	317	0.150	1.68	1.49	3.79	1.41
NiRu0.5	116	299	0.242	1.65	1.46	2.45	1.38
NiRu0.7	113	305	0.362	1.94	1.73	2.61	1.63
NiRu1.0	112	291	0.338	1.96	1.65	1.71	1.64
Ru1.0	122	/	0.305	/	1.54	1.54	/

[a] first peak.
[b] second peak.

disappear on Ru1.0. In conclusion, Ru addition to Ni/CeO_2 reduces the overall acidity of the catalysts, mainly the medium one. With respect to the literature results [78–83] a straightforward comparison is very difficult due to the very different findings reported. For instance, more complex desorption profiles and larger NH_3 desorbed amounts (about 1 mmol/g) are reported on Ni/CeO_2 catalysts by Zhao et al. [79]; moreover, in this work the main contribution is related to strong acid sites. On the contrary, Ni et al. [84] on their Ni/CeO_2 reported the dominance of weak acid sites (no quantitative analysis is reported).

CO_2 TPD provides information about not only basic sites, but also the interaction between a reaction product (CO_2) and the catalyst surface. Ru1.0 shows a wide desorption that can be divided into two large peaks at about 330 and 500 °C. Ni shows a well-defined desorption at low temperatures, fitted with two peaks at about 90 and 150 °C, and a wide peak at about 400 °C. Ru addition to Ni/CeO_2 results in a reduction of the basicity of the sample, as occurred for the acidity. In particular, the

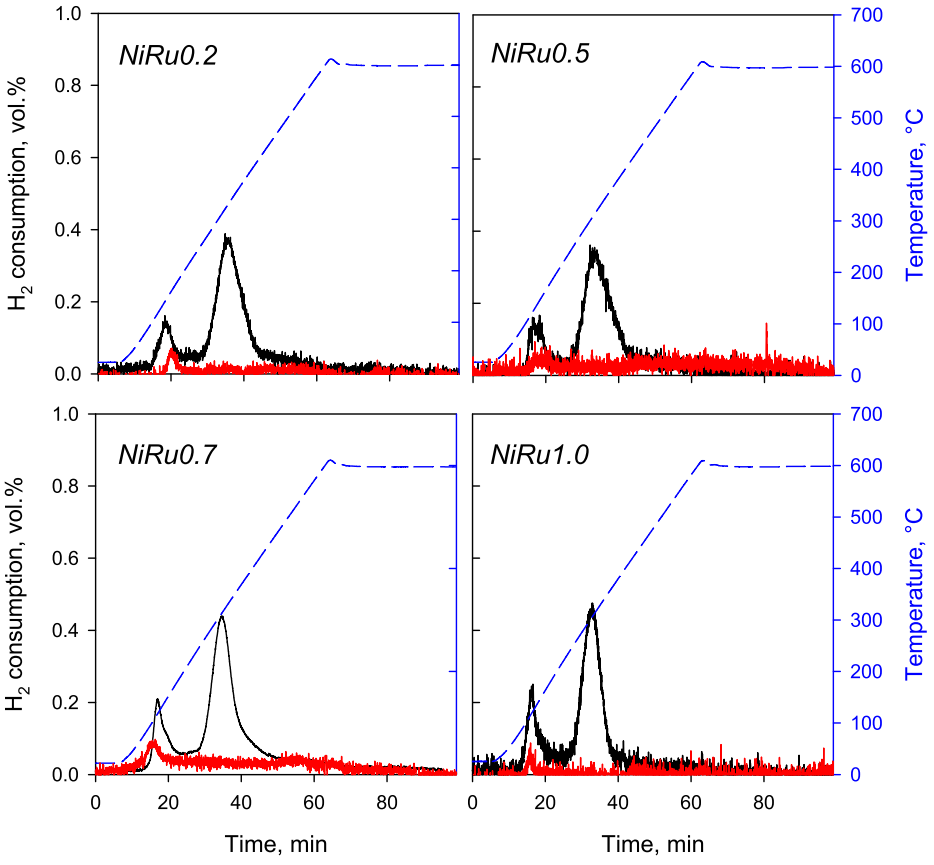

Fig. 5. H_2-TPR profiles on fresh (black lines) and used (red lines) NiRu catalysts. (For interpretation of the references to colour in this figure legend, the reader is referred to the Web version of this article.)

Table 4
Peak temperatures (°C), NH_3 and CO_2 uptakes (mmol/g) for used catalysts.

		Ni		Ru1.0		NiRu1.0	
		Temp.	Amount	Temp.	Amount	Temp.	Amount
NH_3	Peak	91	$5.83{\cdot}10^{-3}$	113	$2.66{\cdot}10^{-3}$	86	$4.24{\cdot}10^{-3}$
	Peak	205	$1.36{\cdot}10^{-2}$	250	$1.83{\cdot}10^{-2}$	285	$2.12{\cdot}10^{-2}$
	Peak	322	$1.49{\cdot}10^{-2}$	432	$7.49{\cdot}10^{-3}$	331	$4.12{\cdot}10^{-3}$
	Peak	517	$6.28{\cdot}10^{-3}$	–	–	537	$1.03{\cdot}10^{-2}$
	Overall	-	$\mathbf{4.02{\cdot}10^{-2}}$	-	$\mathbf{2.84{\cdot}10^{-2}}$	-	$\mathbf{3.99{\cdot}10^{-2}}$
CO_2	Peak	92	$6.04{\cdot}10^{-3}$	–	–	93	$5.15{\cdot}10^{-3}$
	Peak	155	$6.18{\cdot}10^{-3}$	–	–	170	$6.52{\cdot}10^{-3}$
	Peak	393	$1.77{\cdot}10^{-2}$	333	$1.07{\cdot}10^{-2}$	–	–
	Peak			507	$6.84{\cdot}10^{-3}$	487	$3.17{\cdot}10^{-3}$
	Overall	-	$\mathbf{3.03{\cdot}10^{-2}}$	-	$\mathbf{1.75{\cdot}10^{-2}}$	-	$\mathbf{1.48{\cdot}10^{-2}}$

strong basicity, detectable at high temperatures, is significantly reduced. This suggests that CO_2 more easily desorbs from the dual metal catalyst with respect to Ni sample. Our results are similar to those reported by Ma et al. [84] from both the qualitative and quantitative points of view. Actually, assigning each peak to a specific component of the catalyst (i.e. Ni, Ru, CeO_2) is quite difficult. As a matter of fact, CO_2 desorption at low temperatures has been related to both Ni [85,86] and CeO_2 [81,84,87,88]. Pan et al. [85] addressed CO_2 desorption at medium temperatures (300–700 °C) to ceria-zirconia support.

3.3. Steady-state catalytic tests

Steady-state catalytic tests were carried out under the same process conditions ($\tau = 0.08$ g s cm^{-3}, T = 450–550 °C) to assess the effect of Ru loading on the SR activity. Fig. 6 shows the results at different feed compositions and the corresponding equilibrium values.

The monometallic catalysts (especially Ni) show the lowest catalytic activity. By increasing the Ru content in the Ni–Ru catalysts, the catalytic activity increases; the effect does not appear additive, thus suggesting a promotional effect of ruthenium and/or a synergy between the two metals. At the lowest reactant partial pressures (Fig. 6a), the NiRu0.7 catalyst is the most effective, showing methane conversions approaching the steam reforming equilibriumvalue. The NiRu1.0 catalyst shows a similar behaviour. By increasing the steam partial pressure (Fig. 6b), a reduction of the conversions is found, despite more favorable thermodynamic conditions, due to an inhibiting effect of water on the catalytic kinetics. This effect depends on the Ru content: the higher the Ru content, the lower the conversion reduction. Accordingly, the NiRu1.0 catalyst becomes the most active, achieving higher conversions compared to the samples with lower ruthenium loading. By increasing the methane concentration at fixed H_2O/CH_4 ratios (Fig. 6c and d), a slight but not negligible inhibiting effect of methane content is found. Even at higher CH_4 concentration, the positive effect of the Ru content on the inhibiting effect of the steam partial pressure can be evidenced.

Under the above reaction conditions, methane conversions do not generally reach those corresponding to the equilibrium values. However, it is well known that the product distribution depends not only on methane conversion to CO and H_2 but also on the water gas shift reaction.

To evaluate the extent of the WGS reaction, CO conversions to CO_2 were calculated and compared to the equilibrium values of the WGS reaction alone.

Fig. 7 shows the CO conversion as obtained over two samples under different reaction conditions (NiRu0.2 at 3% CH_4 and 6%H_2O; NiRu0.7 at 4% CH_4 and 8% H_2O). CO conversions through WGS reach the thermodynamic equilibrium at each temperature on both samples, while methane conversions are far from the equilibrium values. This condition is observed for each reaction condition and for each catalyst (not reported). Thus, the overall performance of the system is limited by the kinetics of the steam reforming reaction, while the activity towards the water gas shift reaction is higher. The activity of the water gas shift reaction is significantly improved, also thanks to the intrinsic activity of ceria toward CO oxidation [89].

Table S3 shows the catalytic performance of Ni–Ru catalysts reported in the scientific literature [18,37,45,72]. As often occurring in catalysis, a straightforward comparison among the performance is quite difficult due to the wide range of operating conditions reported. However, comparing the results reported in Table S3 reveals that our catalysts show very good performance, comparable with those of the other catalysts but at lower temperatures.

It is worth noting that a TPO was conducted after various reaction tests (i.e. about 50 h under reaction mixtures), as reported in Section 2.3. No CO_2 production was found, thus suggesting no coke formation during the steam reforming reaction.

3.4. Transient catalytic tests

Despite the H_2-TPR showing no bimetallic interaction between Ni and Ru, a synergic effect between the two metals is found by analyzing the catalytic results. To elucidate the roles of each metal in the catalytic activity, cyclic reduction and oxidation tests in transient regime were performed on the reference powder catalysts.

Tests run on the monometallic Ru catalyst are shown in Fig. 8. By feeding H_2O after a reaction test (Fig. 8a), the catalyst is oxidized and a transient H_2 production is found. Replacing H_2O with CH_4 (Fig. 8b), methane is oxidized to CO and CO_2 and H_2 is also detected as a partial

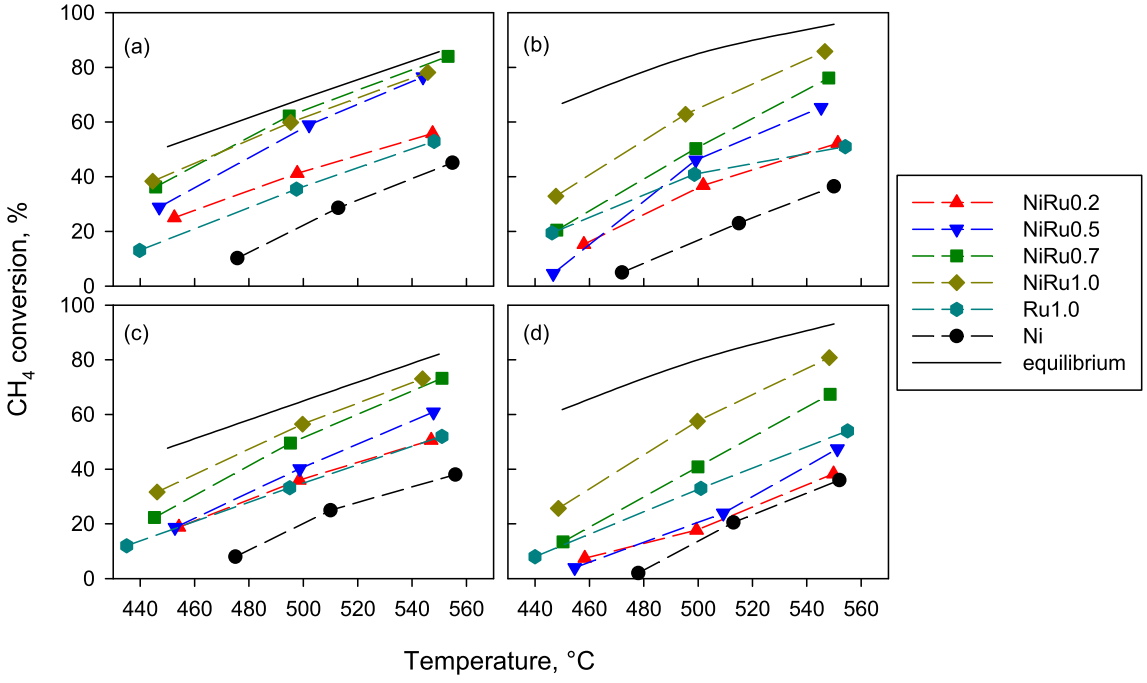

Fig. 6. Effect of the composition of the catalysts and the mixture of the input reagents; (a) 3%CH_4 6%H_2O (b) 3%CH_4 12%H_2O (c) 4%CH_4 8%H_2O (d) 4%CH_4 16% H_2O, Nitrogen: balance.

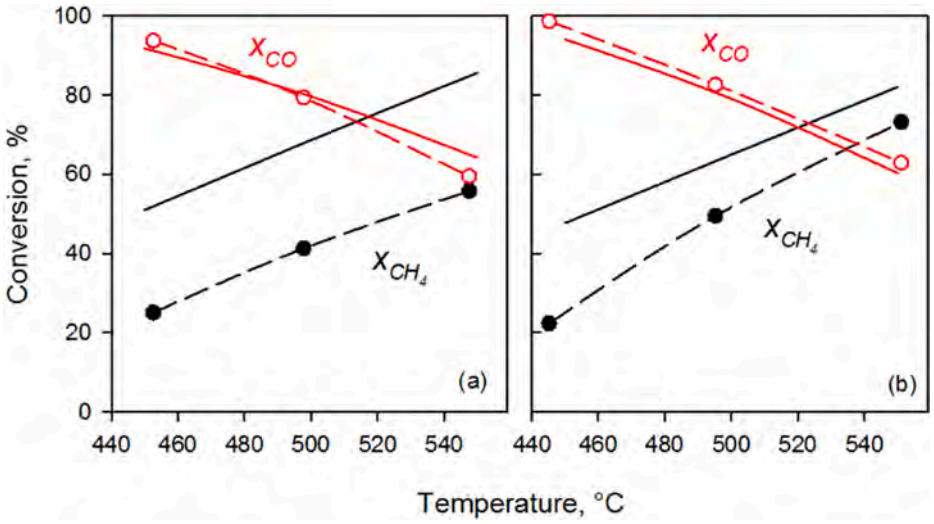

Fig. 7. WGS contribution: (a) 3% CH_4 6%H_2O on NiRu0.2 (b) 4% CH_4 8%H_2O on NiRu0.7, solid lines represent equilibrium conversion.

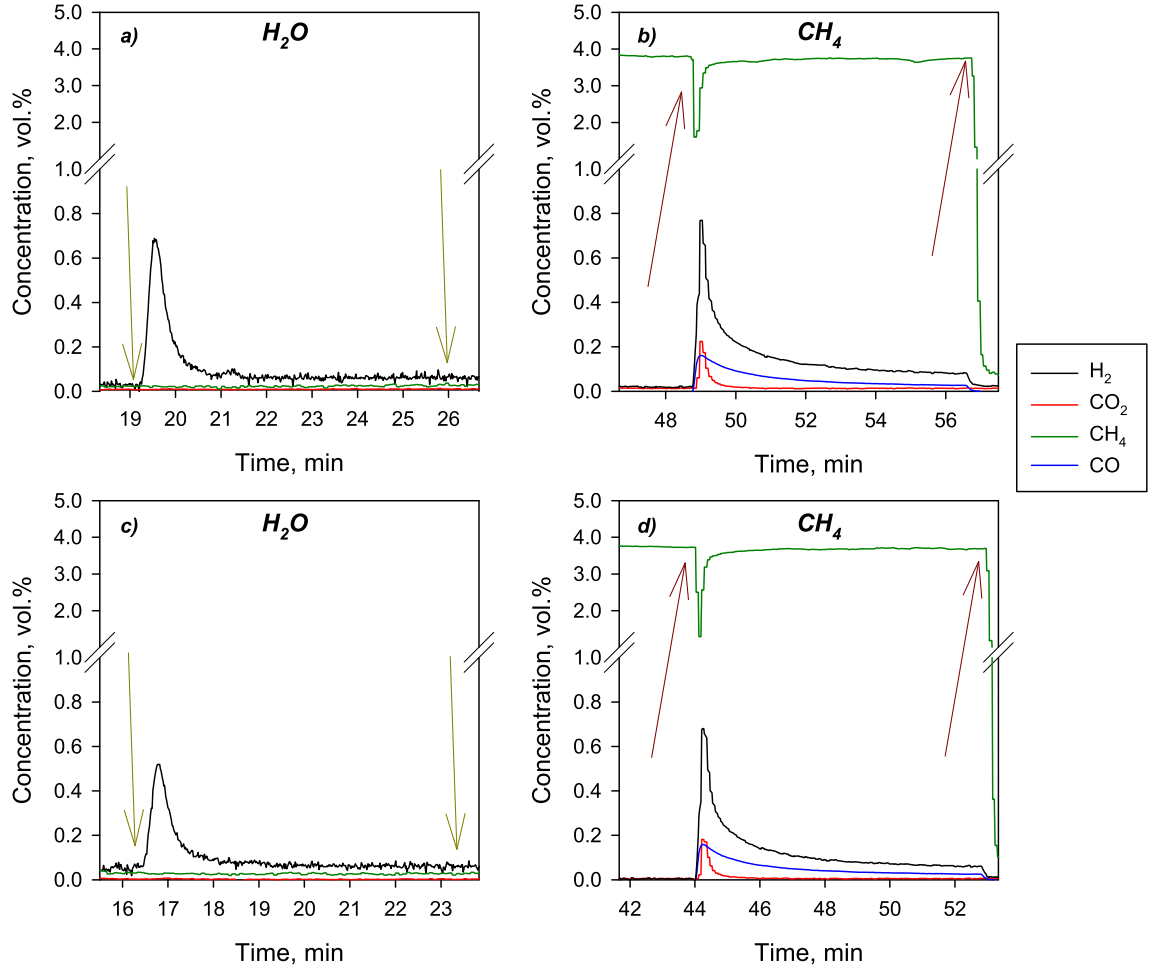

Fig. 8. Cyclic oxidation and reduction tests in transient regime on monometallic Ru catalyst. Arrows indicate the time when the reaction environment is modified.

oxidation product. By feeding H_2O again (Fig. 8c), H_2 is produced, while no CO_x are detected in the exiting stream, suggesting no coke formation during the previous reduction in the CH_4 atmosphere. A further reduction under CH_4 (Fig. 8d) shows a very similar trend to the previous cycle, suggesting no coke formation and a repeatable behavior of this catalyst under the adopted cyclic operating conditions.

The results of tests conducted on the monometallic Ni catalyst are shown in Fig. 9. In the first step with H_2O (Fig. 9a), the behavior is similar to that observed on the Ru catalyst, i.e. mild oxidation of the catalyst with consequent hydrogen formation and negligible formation of CO and CO_2. During the first reduction phase with methane (Fig. 9b), a transient phase is observed where H_2, CO, and CO_2 are formed,

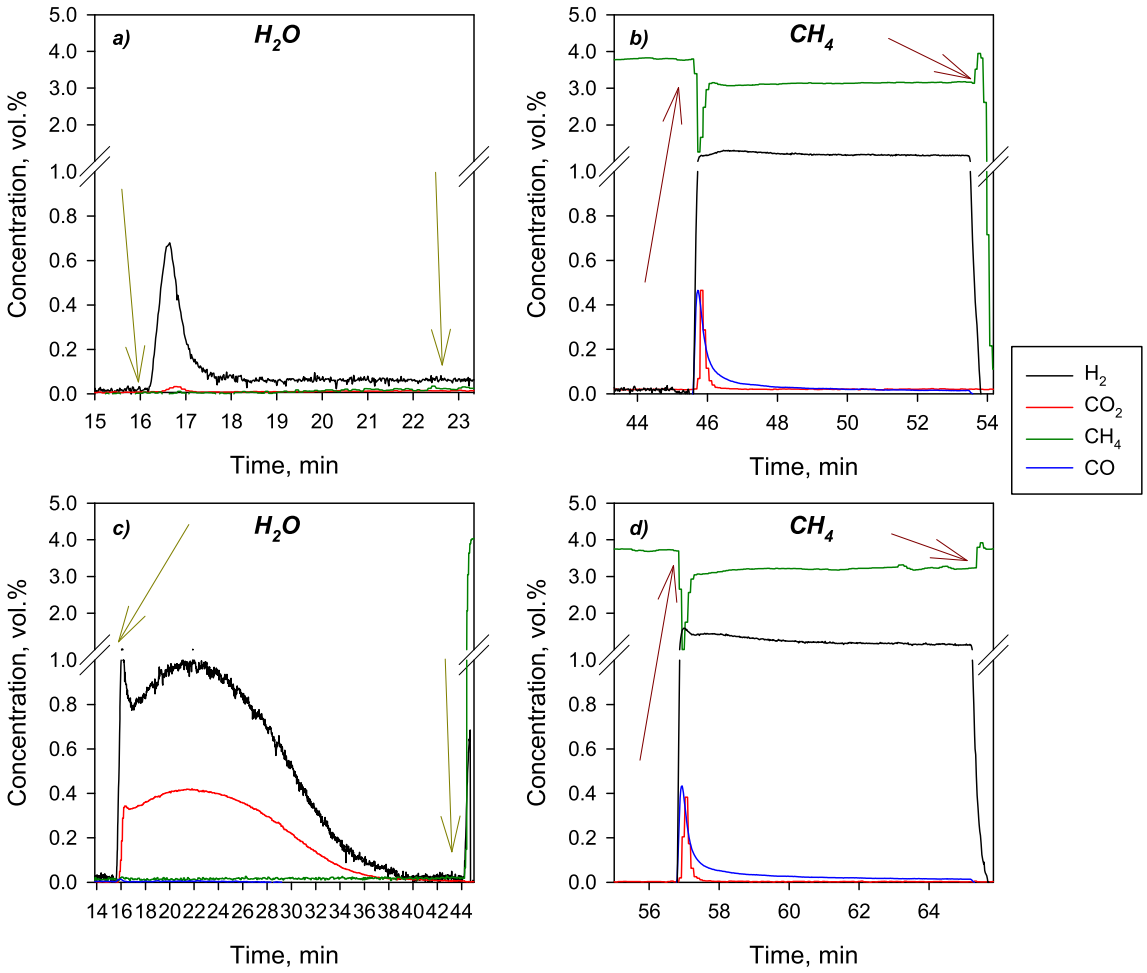

Fig. 9. Cyclic oxidation and reduction tests in transient regime on monometallic Ni catalyst. Arrows indicate the time when the reaction environment is modified.

followed by a second phase (not detected on the Ru catalyst) in which the consumption of methane and the simultaneous production of H_2 cannot be associated with the production of CO and CO_2. Methane is decomposed into H_2 and C, as expected on Ni-based catalysts [90]. By re-feeding H_2O (Fig. 9c), simultaneous production of H_2 and CO_2 due to coke gasification is found. CO production is very low, probably due to ceria activity towards CO oxidation. By re-feeding methane (Fig. 9d) a behavior similar to the first reduction step is found.

Fig. 10 shows the H_2O oxidation and CH_4 reduction steps on NiRu0.7; the other Ni–Ru catalysts exhibit similar behaviors (Figures S9-S11 in Supplementary Material). From a qualitative point of view, the behavior of Ni–Ru catalysts is similar to that observed on monometallic Ni catalyst: H_2 production during the first oxidation step (Fig. 10a), CO and CO_2 production at the beginning of the first reduction step, followed by methane decomposition (Fig. 10b), large CO_2 and H_2 production with negligible CO formation during the second oxidation step (Fig. 10c), a second reduction step in CH_4 similar to the first reduction step (Fig. 10d).

The quantitative analysis of the above experiments is reported in Table 5, confirming the qualitative analysis reported above. In particular, during the oxidation steps under H_2O, more than 99% of CO_x produced is CO_2, while during CH_4 feeding on Ni-containing catalysts the CO/CO_2 ratio is about 4:1. Moreover, it is worth noting that, in the absence of H_2O, methane is mainly converted to coke on monometallic Ni and NiRu catalysts (selectivity to CO_x calculated on CH_4 conversion $\leq$10%; i.e. coke selectivity $\geq$90%). It is worth noting that, considering the first reduction and the second oxidation step, the carbon mass balance was closed within ±8%, which is a good result, taking into account the uncertainty of the experimental procedure here proposed, confirming that all the coke deposited during CH_4 reduction is converted to CO_2 during H_2O oxidation. On Ru1.0, the carbon balance on each reduction step is closed ±5%, i.e. converted methane is fully balanced by produced CO_x, confirming that no coke deposition occurs.

Initial production rates were calculated (Fig. 11) according to the procedure reported in the Supplementary Materials (Section S3.2). It was found that they do not depend on coke content but only on oxygen availability. Reaction rates increase linearly with the Ru content, and the ratio ($\Delta H_2/\Delta CO_2$) is approximately 2, in line with the stoichiometry of the step: $C + 2H_2O \rightarrow CO_2 + 2H_2$.

On the monometallic Ru-based catalyst, there is no coke formation during the reduction phase.

All the characterizations reported in the previous Sections explored the metal-metal and metal-support interactions. The partial incorporation of Ru into the ceria lattice has been revealed from XRD and XPS results, whereas the presence of Ni highly dispersed and in intimate contact with the support has been revealed by XPS and H_2-TPR characterizations. In addition, TEM analysis confirmed the high intimacy of Ru and Ni metals. The combination of the above results suggests a limited formation of bi(multi)-metallic structures, while each metal (Ni and Ru) strongly interacts with ceria. Notwithstanding, redox properties of each Ni/ceria couple is affected by the presence of ruthenium and vice versa, as evidenced by H_2-TPR results. These results suggest that each active phase (Ni and Ru) can be positively affect a reaction step (Ni can activate methane decomposition faster than Ru, Ru can activate water dissociation faster than Ni). From these results, it can be inferred that the enhanced catalytic activity of Ni–Ru/CeO_2 catalysts can be attributed to

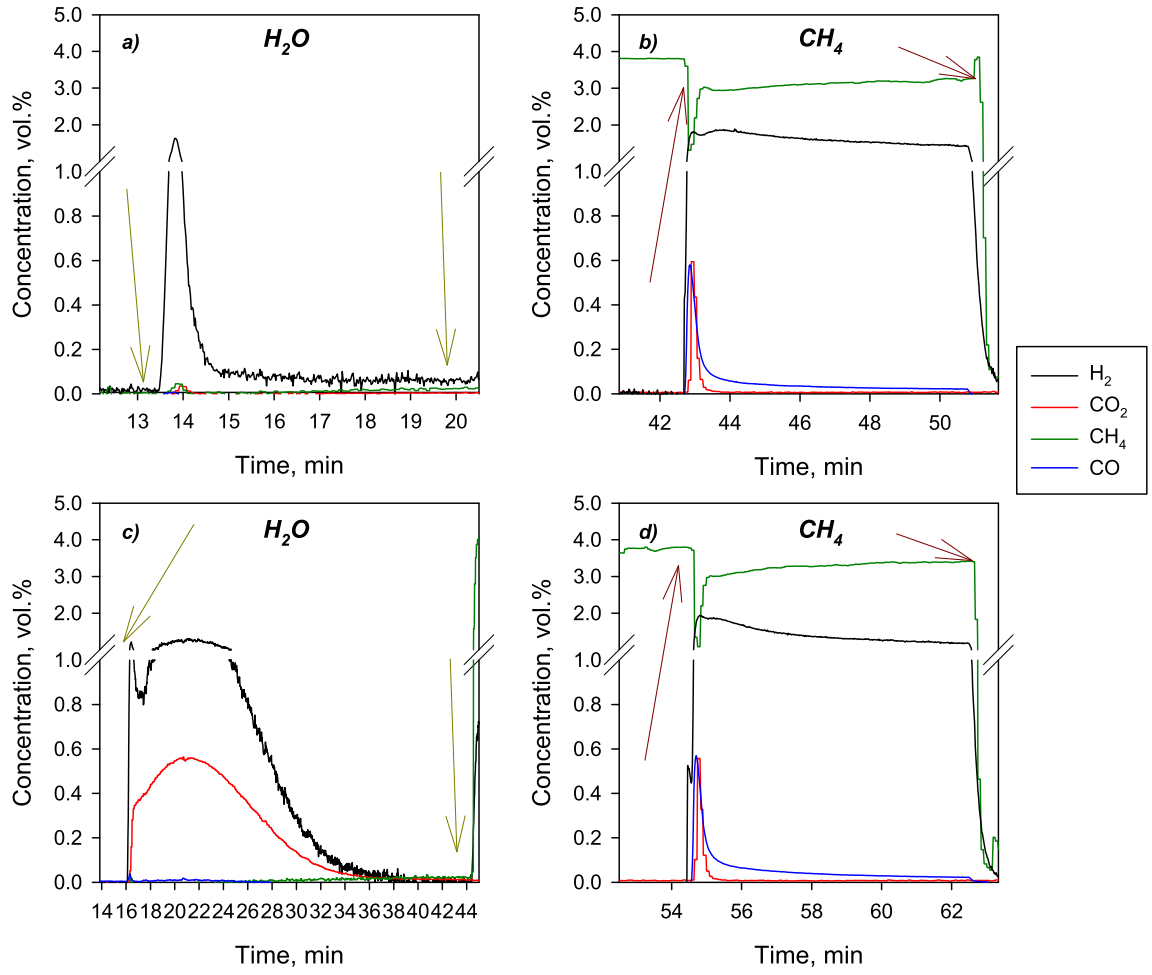

Fig. 10. Cyclic oxidation and reduction tests in transient regime on NiRu0.7 catalyst. Arrows indicate the time when the reaction environment is modified.

Table 5
Quantitative analysis in cyclic oxidation and reduction tests. Selectivities are calculated on CO_x distribution; in brackets, selectivities calculated on methane conversion.

		First cycle			Second cycle		
Sample	**Feed**	x_{CH4}	s_{CO}	s_{CO2}	x_{CH4}	s_{CO}	s_{CO2}
Ni	H_2O/N_2	–	–	–		0.3	99.7
	CH_4/N_2	17	75.0 (3.0)	25.0 (1.0)	14	80.0 (4.0)	20.0 (1.0)
NiRu0.2	H_2O/N_2					0.3	99.7
	CH_4/N_2	19	75.0 (3.0)	25.0 (1.0)	10	77.8 (7.1)	22.2 (1.9)
NiRu0.5	H_2O/N_2					0.5	99.5
	CH_4/N_2	10	80.0 (8.0)	20.0 (2.0)	15	80.0 (4.0)	20.0 (1.0)
NiRu0.7	H_2O/N_2					0.5	99.5
	CH_4/N_2	21	75.0 (3.0)	25.0 (1.0)	17	80.0 (4.0)	20.0 (1.0)
NiRu1.0	H_2O/N_2					0.8	99.2
	CH_4/N_2	14	83.3 (5.0)	16.7 (1.0)	9	81.8 (9.0)	18.2 (2.0)
Ru1.0	H_2O/N_2						
	CH_4/N_2	2%	87.8 (36.0)	12.2 (5.0)	2%	89.1 (41.0)	10.9 (5.0)

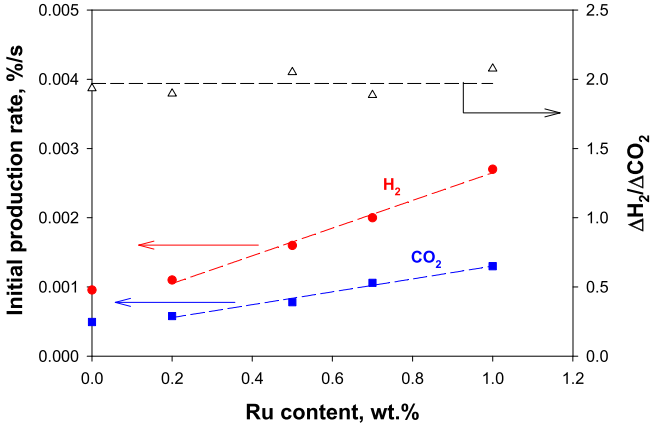

Fig. 11. Initial production rates of H_2 (■) and CO_2 (■) and their ratio $\Delta H_2/\Delta CO_2$ (△) during the oxidation step in H_2O/N_2 as a function of the Ru content.

a cooperative reaction mechanism as follows. Methane is rapidly activated on Ni/CeO_2 sites leading to H_2 and C; the oxidation of C to CO and CO_2 depends on the availability of active oxygen species on the surface, which is improved by the decomposition of H_2O on Ru/CeO_2 sites. The oxygen transfer between the two sites reasonably occurs through the mobility of oxygen on the ceria surface. These results also explain the catalyst's good resistance to fouling.

It is worth noting that the cyclic tests reported above may have a

practical significance. In the reduction phase with methane, there is the production of a high-purity CH_4–H_2 mixture, while a CO_2–H_2 mixture is formed in the oxidation phase with water. This could be beneficial for CO_2 capture, given the low CO content, not requiring further purification steps. From the applicative point of view, the cyclic operation here reported can be compared to chemical looping steam reforming (CLSR). Several results are reported in the literature on this topic [91–94]. However, a full comparison with other Ni-containing materials is not straightforward due to the higher temperature generally used in chemical looping reforming [95–99]. The material composition, the (material weight)-to-(CH_4 flow rate) ratio, the (material weight)-to-(H_2O flow rate) ratio, the time periods of the reduction and oxidation steps significantly affect the methane conversion and the composition of the gaseous streams during the reduction and the oxidation steps (including hydrogen purity during H_2O oxidation). For instance, Ma et al. [96] reported no coke deposition on 5 wt% NiO supported on red mug at 900 °C, allowing pure H_2 production during the H_2O oxidation step. On the contrary, coke formation was reported on other Ni-based materials [95–97].

4. Conclusions

Bi-metallic nickel-ruthenium catalysts supported on ceria by wet impregnation were designed, prepared and tested. The catalyst was designed to obtain a steam methane reforming catalyst more active at relatively low temperatures (below 600 °C) to be used in Pd-based membrane reactors. The catalysts, with low Ni content (7 wt%) and a very low Ru content (≤1 wt%) show good activity towards methane reforming, stable performance, and a good resistance to coke formation. Ruthenium addition not only improves the intrinsic catalytic activity but also enhances the resistance to the inhibiting effect of steam on the reaction rate; the latter is directly related to the ruthenium content.

The CO/CO_2 ratio in the exiting streams appears regulated by the water gas shift equilibrium. This could be related to the CO oxidation activity of ceria at temperatures higher than 400 °C. Moreover, the overall performance appears limited by methane conversion to CO and hydrogen, rather than CO shift to CO_2.

Physico-chemical characterizations suggest that the enhanced catalytic properties of Ni–Ru/CeO_2 catalysts are related to the intimacy between the active metals and their strong-metal-support-interaction with the ceria, resulting in improved redox properties.

Moreover, all the ceria-supported catalysts show self-activation under reaction conditions, thus requiring no pre-treatment under a reducing atmosphere, as generally occurs with Ni-based catalysts.

Declaration of competing interest

The authors declare that they have no known competing financial interests or personal relationships that could have appeared to influence the work reported in this paper.

CRediT authorship contribution statement

G. Sorbino: Data curation, Investigation, Writing – original draft. **A. Di Benedetto:** Formal analysis, Supervision, Writing – review & editing. **C. Italiano:** Data curation, Investigation, Writing – original draft, Writing – review & editing. **M. Thomas:** Data curation, Investigation. **A. Vita:** Supervision, Writing – original draft. **G. Ruoppolo:** Data curation, Validation. **G. Landi:** Conceptualization, Funding acquisition, Methodology, Project administration, Supervision, Validation, Writing – review & editing.

Acknowledgments

This project has received funding from the project "PLUG-IN" (Grant n. 2020N38E75) funded by the MUR Progetti di Ricerca di Rilevante Interesse Nazionale (PRIN) Bando 2020.

The authors gratefully acknowledge Mr. Luciano Cortese (CNR-STEMS) for SEM, Mr. Fernando Stanzione (CNR-STEMS) for ICP-MS analyses, and Mr. Giuseppe Monforte for XPS measurements.

Appendix A. Supplementary data

Supplementary data to this article can be found online at https://doi.org/10.1016/j.ijhydene.2024.07.385.

References

[1] Rasul MG, Hazrat MA, Sattar MA, Jahirul MI, Shearer MJ. The future of hydrogen: challenges on production, storage and applications. Energy Convers Manag 2022; 272:196–8904. https://doi.org/10.1016/j.enconman.2022.116326.

[2] Mohanty US, Ali M, Azhar MR, Al-Yaseri A, Keshavarz A, Iglauer S. Current advances in syngas (CO + H_2) production through bi-reforming of methane using various catalysts: a review. Int J Hydrogen Energy 2021;46:32809–45. https://doi.org/10.1016/j.ijhydene.2021.07.097.

[3] Al-Humaidan FS, Absi Halabi M, Rana MS, Vinoba M. Blue hydrogen: Current status and future technologies. Energy Convers Manag 2023;283:116840. https://doi.org/10.1016/j.enconman.2023.116840.

[4] Iulianelli A, Brunetti A, Pino L, Italiano C, Drago Ferrante G, Gensini M, et al. An integrated two stages inorganic membrane-based system to generate and recover decarbonized H_2 : an experimental study and performance indexes analysis. Renew Energy 2023;210:472–85. https://doi.org/10.1016/j.renene.2023.04.095.

[5] Mamivand S, Binazadeh M, Sohrabi R. Applicability of membrane reactor technology in industrial hydrogen producing reactions: current effort and future directions. J Ind Eng Chem 2021;104:212–30. https://doi.org/10.1016/j.jiec.2021.08.029.

[6] Akamatsu K, Suzuki M, Wang XL, Nakao SI. Hydrogen production by steam reforming of methane in biogas using membrane reactors with dimethoxydimethylsilane-derived silica membranes prepared by chemical vapor deposition. J Chem Eng Jpn 2021;54:387–94. https://doi.org/10.1252/jcej.21we016.

[7] Zhao Q, Su B, Wang H, He A, He R, Kong H, et al. Mid/low-temperature solar hydrogen generation via dry reforming of methane enhanced in a membrane reactor. Energy Convers Manag 2021;240:114254. https://doi.org/10.1016/j.enconman.2021.114254.

[8] Zhang H, Sun Z, Hu YH. Steam reforming of methane: current states of catalyst design and process upgrading. Renew Sustain Energy Rev 2021;149:111330. https://doi.org/10.1016/j.rser.2021.111330.

[9] Wang S, Shen Z, Osatiashtiani A, Ali S, Clough PT. Ni-based bimetallic catalysts for hydrogen production via (sorption-enhanced) steam methane reforming. Chem Eng J 2024;486:150170. https://doi.org/10.1016/j.cej.2024.150170.

[10] Hasnain SMW ul, Farooqi AS, Ayodele BV, Farooqi AS, Sanaullah K, Abdullah B. Advancements in Ni and Co-based catalysts for sustainable syngas production via Bi-reforming of methane: a review of recent advances. J Clean Prod 2024;434:139904. https://doi.org/10.1016/J.JCLEPRO.2023.139904.

[11] Wang S, Nabavi SA, Clough PT. A review on bi/polymetallic catalysts for steam methane reforming. Int J Hydrogen Energy 2023;48:15879–93. https://doi.org/10.1016/J.IJHYDENE.2023.01.034.

[12] Yusuf BO, Umar M, Kotob E, Abdulhakam A, Taialla OA, Awad MM, et al. Recent advances in bimetallic catalysts for methane steam reforming in hydrogen production: current trends, challenges, and future prospects. Chem Asian J 2023; 2023:e202300641. https://doi.org/10.1002/ASIA.202300641.

[13] Estalkhi MH, Yousefpour M, Koohestan H, Taherian Z. Catalytic evaluation of Ni-3% Sr-/MCM-41 in dry and steam reforming of methane. Int J Hydrogen Energy 2024;68:1344–51. https://doi.org/10.1016/j.ijhydene.2024.04.347.

[14] De Souza VP, Costa D, Dos Santos D, Sato AG, Bueno JMC. Pt-promoted α-Al_2O_3-supported Ni catalysts: effect of preparation conditions on oxi-reduction and catalytic properties for hydrogen production by steam reforming of methane. Int J Hydrogen Energy 2012;37:9985–93. https://doi.org/10.1016/j.ijhydene.2012.03.141.

[15] Zhou L, Guo Y, Chen J, Sakurai M, Kameyama H. Trace precious metal Pt doped plate-type anodic alumina Ni catalysts for methane reforming reaction. Fuel 2012; 92:373–6. https://doi.org/10.1016/j.fuel.2011.06.039.

[16] Morales-Cano F, Lundegaard LF, Tiruvalam RR, Falsig H, Skjøth-Rasmussen MS. Improving the sintering resistance of Ni/Al_2O_3 steam-reforming catalysts by promotion with noble metals. Appl Catal Gen 2015;498:117–25. https://doi.org/10.1016/j.apcata.2015.03.016.

[17] Lee SM, Hong SC. Effect of palladium addition on catalytic activity in steam methane reforming over Ni-YSZ porous membrane. Int J Hydrogen Energy 2014; 39:21037–43. https://doi.org/10.1016/j.ijhydene.2014.10.054.

[18] Baek SC, Jun KW, Lee YJ, Kim JD, Park DY, Lee KY. Ru/Ni/$MgAl_2O_4$ catalysts for steam reforming of methane: effects of Ru content on self-activation property. Res Chem Intermed 2012;38:1225–36. https://doi.org/10.1007/s11164-011-0462-0.

[19] Ighalo JO, Amama PB. Recent advances in the catalysis of steam reforming of methane (SRM). Int J Hydrogen Energy 2024;51:688–700. https://doi.org/10.1016/j.ijhydene.2023.10.177.

[20] de Oliveira Rocha K, Marques CMP, Bueno JMC. Effect of Au doping of Ni/Al_2O_3 catalysts used in steam reforming of methane: mechanism, apparent activation

energy, and compensation effect. Chem Eng Sci 2019;207:844–52. https://doi.org/10.1016/j.ces.2019.06.049.
[21] Wang H, Blaylock DW, Dam AH, Liland SE, Rout KR, Zhu YA, et al. Steam methane reforming on a Ni-based bimetallic catalyst: density functional theory and experimental studies of the catalytic consequence of surface alloying of Ni with Ag. Catal Sci Technol 2017;7:1713–25. https://doi.org/10.1039/c7cy00101k.
[22] Xu Y, Fan C, Zhu YA, Li P, Zhou XG, Chen D, et al. Effect of Ag on the control of Ni-catalyzed carbon formation: a density functional theory study. Catal Today 2012;186:54–62. https://doi.org/10.1016/j.cattod.2011.08.041.
[23] Nazari M, Alavi SM. An investigation of the simultaneous presence of Cu and Zn in different Ni/Al_2O_3 catalyst loads using Taguchi design of experiment in steam reforming of methane. Int J Hydrogen Energy 2020;45:691–702. https://doi.org/10.1016/j.ijhydene.2019.10.224.
[24] Li MR, Lu Z, Wang GC. The effect of potassium on steam-methane reforming on the Ni_4/Al_2O_3 surface: a DFT study. Catal Sci Technol 2017;7:3613–25. https://doi.org/10.1039/c7cy00986k.
[25] Liang D, Wang Y, Chen M, Xie X, Li C, Wang J, et al. Dry reforming of methane for syngas production over attapulgite-derived MFI zeolite encapsulated bimetallic Ni-Co catalysts. Appl Catal B Environ 2023;322:122088. https://doi.org/10.1016/j.apcatb.2022.122088.
[26] Jeong JH, Lee JW, Seo DJ, Seo Y, Yoon WL, Lee DK, et al. Ru-doped Ni catalysts effective for the steam reforming of methane without the pre-reduction treatment with H2. Appl Catal Gen 2006;302:151–6. https://doi.org/10.1016/j.apcata.2005.12.007.
[27] Li D, Nishida K, Zhan Y, Shishido T, Oumi Y, Sano T, et al. Superior catalytic behavior of trace Pt-doped Ni/Mg(Al)O in methane reforming under daily start-up and shut-down operation. Appl Catal Gen 2008;350:225–36. https://doi.org/10.1016/j.apcata.2008.08.017.
[28] Li D, Zhan Y, Nishida K, Oumi Y, Sano T, Shishido T, et al. "Green" preparation of "intelligent" Pt-doped Ni/Mg(Al)O catalysts for daily start-up and shut-down CH_4 steam reforming. Appl Catal Gen 2009;363:169–79. https://doi.org/10.1016/j.apcata.2009.05.015.
[29] Miyata T, Li D, Shiraga M, Shishido T, Oumi Y, Sano T, et al. Promoting effect of Rh, Pd and Pt noble metals to the Ni/Mg(Al)O catalysts for the DSS-like operation in CH_4 steam reforming. Appl Catal Gen 2006;310:97–104. https://doi.org/10.1016/j.apcata.2006.05.022.
[30] Li D, Shishido T, Oumi Y, Sano T, Takehira K. Self-activation and self-regenerative activity of trace Rh-doped Ni/Mg(Al)O catalysts in steam reforming of methane. Appl Catal Gen 2007;332:98–109. https://doi.org/10.1016/j.apcata.2007.08.008.
[31] Miyata T, Shiraga M, Li D, Atake I, Shishido T, Oumi Y, et al. Promoting effect of Ru on Ni/Mg(Al)O catalysts in DSS-like operation of CH_4 steam reforming. Catal Commun 2007;8:447–51. https://doi.org/10.1016/j.catcom.2006.07.018.
[32] Li D, Atake I, Shishido T, Oumi Y, Sano T, Takehira K. Self-regenerative activity of Ni/Mg(Al)O catalysts with trace Ru during daily start-up and shut-down operation of CH_4 steam reforming. J Catal 2007;250:299–312. https://doi.org/10.1016/j.jcat.2007.06.002.
[33] Kim T, Lee J, Jo S, Kim J, Woo J, Dhanusuraman R, et al. Improving the stability of Ru-doped Ni-based catalysts for steam methane reforming during daily startup and shutdown operation. Catalysts 2023;13(6):949. https://doi.org/10.3390/catal13060949.
[34] Fazlikeshteli S, Vendrell X, Llorca J. Catalytic partial oxidation of methane over bimetallic Ru-Ni supported on CeO_2 for syngas production. Int J Hydrogen Energy 2023;51:1494–507. https://doi.org/10.1016/j.ijhydene.2023.07.349.
[35] Ibrahim AA, Al-Fatesh AS, Alwadai N, Abasaeed AE, Al-Zahrani SA, Abu-Dahrieh JK, Abasaeed AE. Promotion impact of different strontium doping on Ni-9La+Zr catalyst for dry reforming of methane. Energy Sci Eng 2023:4625–34. https://doi.org/10.1002/ese3.1604.
[36] Kumar R, Kumar K, Choudary NV, Pant KK. Effect of support materials on the performance of Ni-based catalysts in tri- reforming of methane. Fuel Process Technol 2019;186:40–52. https://doi.org/10.1016/j.fuproc.2018.12.018.
[37] Gubareni IV, Kurilets YP, Soloviev SO. Effect of additives La_2O_3 and CeO_2 on the activity and selectivity of $Ni-Al_2O_3$/cordierite catalysts in steam reforming of methane. Theor Exp Chem 2014;50:311–7. https://doi.org/10.1007/s11237-014-9381-7.
[38] Alli RD, Souza PAL De, Mohamedali M, Virla LD, Mahinpey N. Tri-reforming of methane for syngas production using Ni catalysts : current status and future outlook. Catal Today 2023;407:107–24. https://doi.org/10.1016/j.cattod.2022.02.006.
[39] Manan WN, Wan Isahak WNR, Yaakob Z. CeO_2-Based heterogeneous catalysts in dry reforming methane and steam reforming methane: a short review. Catalysts 2022;12:452. https://doi.org/10.3390/CATAL12050452. 2022;12:452.
[40] García-Vargas JM, Valverde JL, Dorado F, Sánchez P. Influence of the support on the catalytic behaviour of Ni catalysts for the dry reforming reaction and the tri-reforming process. Journal Mol Catal A, Chem 2014;395:108–16. https://doi.org/10.1016/j.molcata.2014.08.019.
[41] Dai Y, Zou R, Ba T, Zhang J, Liu C. Highly active and coke resistant $Ni/CeZrO_2$ catalyst prepared by cold plasma decomposition for CO_2 reforming of methane. J CO_2 Util 2021;51:101647. https://doi.org/10.1016/j.jcou.2021.101647.
[42] Lustemberg PG, Ram PJ, Liu Z, Grinter DG, Carrasco J, Senanayake SD, Rodriguez JA. Ganduglia-pirovano MV room-temperature activation of methane and dry Re-forming with CO_2 on Ni-CeO_2 (111) surfaces: effect of Ce^{3+} sites and metal-support interactions on C-H bond cleavage. ACS Catal 2016;6:8184–91. https://doi.org/10.1021/acscatal.6b02360.
[43] Bian Z, Xia H, Jiang B, Wang Z, Yu Y, Yu K, et al. A CFD study on H_2-permeable membrane reactor for methane CO_2 reforming: effect of catalyst bed volume. Int J Hydrogen Energy 2021;46:38336–50. https://doi.org/10.1016/j.ijhydene.2021.09.098.
[44] Current Heraeus Precious Metals Prices n.d. https://www.heraeus.com/en/hpm/pm_prices/prices/current_hu.html (accessed January 14, 2024).
[45] Zakrzewski M, Shtyka O, Ciesielski R, Kedziora A, Maniukiewicz W, Arcab N, et al. Effect of ruthenium and cerium oxide (IV) promotors on the removal of carbon deposit formed during the mixed methane reforming process. Materials 2021;14:7581. https://doi.org/10.3390/ma14247581.
[46] García-Vargas JM, Valverde JL, De Lucas-Consuegra A, Gómez-Monedero B, Sánchez P, Dorado F. Precursor influence and catalytic behaviour of Ni/CeO_2 and Ni/SiC catalysts for the tri-reforming process. Appl Catal Gen 2012;431–432:49–56. https://doi.org/10.1016/j.apcata.2012.04.016.
[47] Italiano C, Ashraf MA, Pino L, Moncada Quintero CW, Specchia S, Vita A. Rh/CeO_2 thin catalytic layer deposition on alumina foams: catalytic performance and controlling regimes in biogas reforming processes. Catalysts 2018;8. https://doi.org/10.3390/catal8100448.
[48] Vita A, Cristiano G, Italiano C, Pino L, Specchia S. Syngas production by methane oxy-steam reforming on Me/CeO_2 (Me=Rh, Pt, Ni) catalyst lined on cordierite monoliths. Appl Catal B Environ 2015;162:551–63. https://doi.org/10.1016/j.apcatb.2014.07.028.
[49] Shen Z, Nabavi SA, Clough PT. Design and performance testing of a monolithic nickel-based SiC catalyst for steam methane reforming. Appl Catal A, Gen 2024;670:119529. https://doi.org/10.1016/j.apcata.2023.119529.
[50] Landi G, Barbato PS, Di Benedetto A, Pirone R, Russo G. High pressure kinetics of CH_4, CO and H_2 combustion over $LaMnO_3$ catalyst. Appl Catal, B 2013;134–135:110–22. https://doi.org/10.1016/j.apcatb.2012.12.040.
[51] Luciani G, Landi G, Aronne A, Di Benedetto A. Partial substitution of B cation in $La_{0.6}Sr_{0.4}MnO_3$ perovskites: a promising strategy to improve the redox properties useful for solar thermochemical water and carbon dioxide splitting. Sol Energy 2018;171:1–7. https://doi.org/10.1016/j.solener.2018.06.058.
[52] Landi G, Barbato PS, Di Benedetto A, Lisi L. Optimization of the preparation method of CuO/CeO_2 structured catalytic monolith for CO preferential oxidation in H_2-rich streams. Appl Catal, B 2016;181:727–37. https://doi.org/10.1016/j.apcatb.2015.08.040.
[53] Baek SC, Jun KW, Lee YJ, Kim JD, Park DY, Lee KY. Ru/Ni/$MgAl_2O_4$ catalysts for steam reforming of methane: effects of Ru content on self-activation property. Res Chem Intermed 2012;38:1225–36. https://doi.org/10.1007/s11164-011-0462-0.
[54] Tsiotsias AI, Charisiou ND, Italiano C, Ferrante GD, Pino L, Vita A, et al. Ni-noble metal bimetallic catalysts for improved low temperature CO_2 methanation. Appl Surf Sci 2024;646. https://doi.org/10.1016/j.apsusc.2023.158945.
[55] Woo R, Lee K, An BS, Kim SH, Ju HK, Kim JH, et al. $BaCeO_3$ perovskite-incorporated Co catalyst for efficient NH_3 synthesis under mild conditions. Chem Eng J 2023;475:146354. https://doi.org/10.1016/j.cej.2023.146354.
[56] Zhang T, Zheng P, Gu F, Xu W, Chen W, Zhu T, et al. The dual-active-site tandem catalyst containing Ru single atoms and Ni nanoparticles boosts CO_2 methanation. Appl Catal, B 2023;323:122190. https://doi.org/10.1016/j.apcatb.2022.122190.
[57] Alves LMNC, Almeida MP, Ayala M, Watson CD, Jacobs G, Rabelo-Neto RC, et al. CO_2 methanation over metal catalysts supported on ZrO_2: effect of the nature of the metallic phase on catalytic performance. Chem Eng Sci 2021;239:116604. https://doi.org/10.1016/j.ces.2021.116604.
[58] Li P, Zhang M. MOF-derived NiO/CeO_2 heterojunction : a photocatalyst for degrading pollutants and hydrogen evolution. J Mater Sci 2020;55:15930–44. https://doi.org/10.1007/s10853-020-05123-2.
[59] Hassannejad H, Mele C, Shahrabi T. Electrodeposition of Ni/Ceria composites: an in situ visible reflectance investigation. J Solid State Electrochem 2012;16:3429. https://doi.org/10.1007/s10008-012-1830-4.
[60] Channei D, Inceesungvorn B, Wetchakun N, Ukritnukun S, Nattestad A, Chen J. Photocatalytic Degradation of Methyl Films under Visible Light Irradiation https://doi.org/10.1038/srep05757.
[61] Vita A, Italiano C, Pino L, Frontera P, Ferraro M. Activity and stability of powder and monolith-coated Ni/GDC catalysts for CO_2 methanation. Appl Catal B Environ 2018;226:384–95. https://doi.org/10.1016/j.apcatb.2017.12.078.
[62] Larachi F, Pierre J, Adnot A, Bernis A. Ce 3d XPS study of composite $Ce_xMn_{1-x}O_{2-y}$ wet oxidation catalysts. Appl Surf Sci 2002;195:236–50. https://doi.org/10.1016/S0169-4332(02)00559-7.
[63] Du Y-R, Wang R, Niu Q-S, Tao Y-Y, Xu B-H. Ru-Ni bimetallic catalyst supported on CeO_2 boosts chemoselective methoxycarbonylation of olefins. Chem Eng J 2024;488:151020. https://doi.org/10.1016/j.cej.2024.151020.
[64] Zhang T, Zheng P, Gao J, Han Z, Gu F, Xu W, Wang F, Zhu T, Xu G, Zhong Z. Su F Self-dispersed bimetallic NiRu nanoparticles on CeO_2 for CO_2 methanation. Chem Eng J 2024;481:148548. https://doi.org/10.1016/j.cej.2024.148548.
[65] Chen D, He D, Lu J, Zhong L, Liu F, Liu J, et al. Investigation of the role of surface lattice oxygen and bulk lattice oxygen migration of cerium-based oxygen carriers: XPS and designed H_2-TPR characterization. Appl Catal B Environ 2017;218:249–59. https://doi.org/10.1016/j.apcatb.2017.06.053.
[66] Rojas JV, Toro-gonzalez M, Molina-higgins MC, Castano CE. Facile radiolytic synthesis of ruthenium nanoparticles on graphene oxide and carbon nanotubes. Mater Sci Eng B 2016;205:28–35. https://doi.org/10.1016/j.mseb.2015.12.005.
[67] Italiano C, Llorca J, Pino L, Ferraro M, Antonucci V, Vita A, et al. Applied Catalysis B : environmental CO and CO_2 methanation over Ni catalysts supported on CeO_2 , Al_2O_3 and Y_2O_3 oxides. Appl Catal B Environ 2020;264:118494. https://doi.org/10.1016/j.apcatb.2019.118494.
[68] Sanz JM, Tyuliev GT. An XPS study of thin NiO films deposited on MgO(100). Surf Sci 1996;367:196–202. https://doi.org/10.1016/S0039-6028(96)00818-7.

[69] Rojas JV, Toro-gonzalez M, Molina-higgins MC, Castano CE. Facile radiolytic synthesis of ruthenium nanoparticles on graphene oxide and carbon nanotubes. Mater Sci Eng B 2016;205:28–35. https://doi.org/10.1016/j.mseb.2015.12.005.
[70] Uskov SI, Potemkin DI, Pakharukova VP, Belyaev VD, Snytnikov PV, Kirillov VA, et al. Activation of a nickel-chromium catalyst for low-temperature steam reforming of C2+-alkanes. Catal Today 2021;378:106–12. https://doi.org/10.1016/j.cattod.2020.11.014.
[71] Mierczynski P, Mosinska M, Stepinska N, Chalupka K, Nowosielska M, Maniukiewicz W, et al. Effect of the support composition on catalytic and physicochemical properties of Ni catalysts in oxy-steam reforming of methane. Catal Today 2021;364:46–60. https://doi.org/10.1016/j.cattod.2020.05.037.
[72] Álvarez MA, Centeno MÁ, Odriozola JA. Ru-Ni catalyst in the combined dry-steam reforming of methane: the importance in the metal order addition. Top Catal 2016; 59:303–13. https://doi.org/10.1007/s11244-015-0426-5.
[73] Zakrzewski M, Shtyka O, Ciesielski R, Kedziora A, Maniukiewicz W, Arcab N, et al. Effect of ruthenium and cerium oxide (IV) promotors on the removal of carbon deposit formed during the mixed methane reforming process. Materials 2021;14: 7581. https://doi.org/10.3390/ma14247581.
[74] Mahfouz R, Estephane J, Gennequin C, Tidahy L, Aouad S, Abi-Aad E. CO_2 reforming of methane over Ni and/or Ru catalysts supported on mesoporous KIT-6: effect of promotion with Ce. J Environ Chem Eng 2021;9:104662. https://doi.org/10.1016/j.jece.2020.104662.
[75] Álvarez MA, Centeno MÁ, Odriozola JA. Ru-Ni catalyst in the combined dry-steam reforming of methane: the importance in the metal order addition. Top Catal 2016; 59:303–13. https://doi.org/10.1007/s11244-015-0426-5.
[76] Zhang J, Zhu D, Yan J, Wang CA. Strong metal-support interactions induced by an ultrafast laser. Nat Commun 2021;12:1–10. https://doi.org/10.1038/s41467-021-27000-5.
[77] Chen J, Zhang Y, Zhang Z, Hou D, Bai F, Han Y, et al. Metal-support interactions for heterogeneous catalysis: mechanisms, characterization techniques and applications. J Mater Chem A Mater 2023;6:4883–5230. https://doi.org/10.1039/D2TA10036C.
[78] Jiang W, Cao JP, Xie JX, Zhao L, Zhang C, Zhao XY, et al. Catalytic hydrodeoxygenation of lignin and its model compounds to hydrocarbon fuels over a metal/acid Ru/HZSM-5 catalyst. Energy Fuel 2021;35:19543–52. https://doi.org/10.1021/ACSENERGYFUELS.1C03169.
[79] Zhao J, Bai X, Wei XY, Dilixiati Y, Lv JH, Kong QQ, et al. Ceria supported nickel nanoparticles for catalytic hydroconversion of lignin-related model compounds. J Solid State Chem 2023;328:124351. https://doi.org/10.1016/J.JSSC.2023.124351.
[80] Qiu S, Xu Y, Weng Y, Ma L, Wang T. Efficient hydrogenolysis of guaiacol over highly dispersed Ni/MCM-41 catalyst combined with HZSM-5. Catalysts 2016;6: 134. https://doi.org/10.3390/CATAL6090134.
[81] Glorius M, Markovits MAC, Breitkopf C. Design of specific acid-base-properties in CeO_2-ZrO_2-mixed oxides via templating and Au modification. Catalysts 2018;8: 358. https://doi.org/10.3390/CATAL8090358.
[82] Wang YW, Zhang YJ, Wang KJ, Tan LM, Chen SY. Preparation of Ni/SiO_2 by ammonia evaporation method for synthesis of 2-MTHF from 2-MF hydrogenation. J Fuel Chem Technol 2021;49:97–103. https://doi.org/10.1016/S1872-5813(21)60007-5.
[83] Ni Z, Djitcheu X, Gao X, Wang J, Liu H, Zhang Q. Effect of preparation methods of CeO_2 on the properties and performance of Ni/CeO_2 in CO_2 reforming of CH_4. Sci Rep 2022;12:1–10. https://doi.org/10.1038/s41598-022-09291-w.
[84] Ma Y, Liu J, Chu M, Yue J, Cui Y, Xu G. Cooperation between active metal and basic support in Ni-based catalyst for low-temperature CO2 methanation. Catal Letters 2020;150:1418–26. https://doi.org/10.1007/S10562-019-03033-W/FIGURES/5.
[85] Pan Q, Peng J, Sun T, Wang S, Wang S. Insight into the reaction route of CO_2 methanation: promotion effect of medium basic sites. Catal Commun 2014;45: 74–8. https://doi.org/10.1016/J.CATCOM.2013.10.034.
[86] Schreiter N, Kirchner J, Kureti S. A DRIFTS and TPD study on the methanation of CO_2 on Ni/Al_2O_3 catalyst. Catal Commun 2020;140:105988. https://doi.org/10.1016/J.CATCOM.2020.105988.
[87] Di Benedetto A, Landi G, Lisi L. Improved CO-PROX performance of CuO/CeO_2 catalysts by using nanometric ceria as support. Catalysts 2018;8. https://doi.org/10.3390/catal8050209.
[88] Barbato PS, Colussi S, Di Benedetto A, Landi G, Lisi L, Llorca J, et al. Origin of high activity and selectivity of CuO/CeO $_2$ catalysts prepared by solution combustion synthesis in CO-prox reaction. J Phys Chem C 2016;120:13039–48. https://doi.org/10.1021/acs.jpcc.6b02433.
[89] Di Sarli V, Landi G, Lisi L, Saliva A, Di Benedetto A. Catalytic diesel particulate filters with highly dispersed ceria: effect of the soot-catalyst contact on the regeneration performance. Appl Catal, B 2016;197:116–24. https://doi.org/10.1016/j.apcatb.2016.01.073.
[90] Karimi S, Bibak F, Meshkani F, Rastegarpanah A, Deng J, Liu Y, et al. Promotional roles of second metals in catalyzing methane decomposition over the Ni-based catalysts for hydrogen production: a critical review. Int J Hydrogen Energy 2021; 46:20435–80. https://doi.org/10.1016/j.ijhydene.2021.03.160.
[91] Dawa T, Sajjadi B. Exploring the potential of perovskite structures for chemical looping technology: a state-of-the-art review. Fuel Process Technol 2024;253: 108022. https://doi.org/10.1016/j.fuproc.2023.108022.
[92] Alamiery A. Advancements in materials for hydrogen production: a review of cutting-edge technologies. ChemPhysMater 2024;3:64–73. https://doi.org/10.1016/j.chphma.2023.09.002.
[93] He J, Yang Q, Song Z, Chang W, Huang C, Zhu Y, et al. Improving the carbon resistance of iron-based oxygen carrier for hydrogen production via chemical looping steam methane reforming: a review. Fuel 2023;351:128864. https://doi.org/10.1016/j.fuel.2023.128864.
[94] Boscherini M, Storione A, Minelli M, Miccio F, Doghieri F. New perspectives on catalytic hydrogen production by the reforming, partial oxidation and decomposition of methane and biogas. Energies 2023;16:6375. https://doi.org/10.3390/EN16176375.
[95] Beom Han S, Sung Kim M, Deng Y, Yeon Kang K, Choi JS, Jang E, et al. Chemical looping-based catalytic CH_4 decomposition and successive coke gasification with CO_2 on ordered mesoporous NiMCeOx (M = Co, Zr, La). Chem Eng J 2024;489: 151034. https://doi.org/10.1016/J.CEJ.2024.151034.
[96] Ma S, Cheng F, Meng J, Ge H, Lu P, Song T. Ni-enhanced red mud oxygen carrier for chemical looping steam methane reforming. Fuel Process Technol 2022;230: 107204. https://doi.org/10.1016/J.FUPROC.2022.107204.
[97] Papalas T, Palamas E, Antzaras AN, Lemonidou AA. Evaluating bimetallic Ni-Co oxygen carriers for their redox behavior and catalytic activity toward steam methane reforming. Fuel 2024;359:130272. https://doi.org/10.1016/J.FUEL.2023.130272.
[98] Guan Y, Liu Y, Song H, Wang B, Zhang G, Wang Y. High-reactive and coke-resistant polyhedral NiO/Fe_2O_3 oxygen carrier for enhancing chemical looping CH_4–CO_2 dry reforming. J Clean Prod 2024;447:141490. https://doi.org/10.1016/J.JCLEPRO.2024.141490.
[99] Quan J, Chen Y, Mai H, Zeng Q, Lv J, Jiang E, et al. Uniformly dispersed $NiFeAlO_4$ as oxygen carrier for chemical looping steam methane reforming to produce syngas. Int J Hydrogen Energy 2024;61:901–13. https://doi.org/10.1016/J.IJHYDENE.2024.02.355.